

# Phase-field modeling of fracture in variably saturated porous media

T. Cajuhi<sup>1</sup> · L. Sanavia<sup>2</sup> · L. De Lorenzis<sup>1</sup>

Received: 1 April 2017 / Accepted: 27 July 2017 / Published online: 7 August 2017  
© Springer-Verlag GmbH Germany 2017

**Abstract** We propose a mechanical and computational model to describe the coupled problem of poromechanics and cracking in variably saturated porous media. A classical poromechanical formulation is adopted and coupled with a phase-field formulation for the fracture problem. The latter has the advantage of being able to reproduce arbitrarily complex crack paths without introducing discontinuities on a fixed mesh. The obtained simulation results show good qualitative agreement with desiccation experiments on soils from the literature.

**Keywords** Porous media mechanics · Fracture · Phase-field modeling · Variably saturated conditions · Desiccation

## 1 Introduction

Porous media mechanics is of great importance e.g. in civil and geo-environmental engineering. Porous media are composed of a solid skeleton and interconnected voids filled with one or more fluids such as air and liquid water. Fluid flow taking place in the pore network can lead to deformation of the solid skeleton and possibly to fracture as observed in hydraulic fracture and desiccation. The ability to numerically simulate these coupled phenomena would support a deeper understanding of the physics involved. Also, a computational model would allow for extensive studies investigating the

influence of the material and hydraulic properties and of the test setup, less expensive than the corresponding experiments.

Cracking due to drying or desiccation can be observed in several porous media such as wood, soils and concrete [1–5]. During drying, a capillary pressure develops within the medium and, consequently, the degree of saturation and the relative permeability vary. When the specimen is mechanically restrained and/or due to pressure gradients, tensile stresses [4,6–9] or shear stresses typically arise [10] leading to cracking [4].

In the literature, drying-induced cracking has been the subject of a number of experimental and modeling studies. A study on the differences between free and constrained drying was performed in [11]. For free shrinkage, the specimen was placed on a polytetrafluoroethylene plate to minimize friction and thus approximate unrestrained conditions. No cracks were observed because the specimen was free to shrink. During constrained desiccation, the authors observed several cracks starting at the upper drying surface and propagating to the bottom of the specimen. Furthermore, cracking starting at the lower corners of the sample was observed, leading to partial detachment of the bottom surface. A schematic representation of these desiccation cracks is shown in Fig. 1, considering a prismatic specimen constrained at the bottom and subjected to drying from the upper and lateral surfaces.

A general review of numerical models for multi-field simulation of fracture can be found in [12]. Desiccation cracks have been numerically modeled by several authors [3,13–16] mostly aiming at a qualitative analysis of the crack patterns in different specimen types. A review on experimental setups, physical behavior and modeling approaches for initially water saturated clayey materials can be found in [17]. In [18,19], the numerical specimen subjected to drying contains

✉ T. Cajuhi  
t.cajuhi@tu-braunschweig.de

<sup>1</sup> Institute of Applied Mechanics, Technische Universität Braunschweig, Pockelsstr. 3, 38106 Braunschweig, Germany

<sup>2</sup> Department of Civil, Architectural and Environmental Engineering, University of Padova, Via Marzolo 9, Padova, Italy

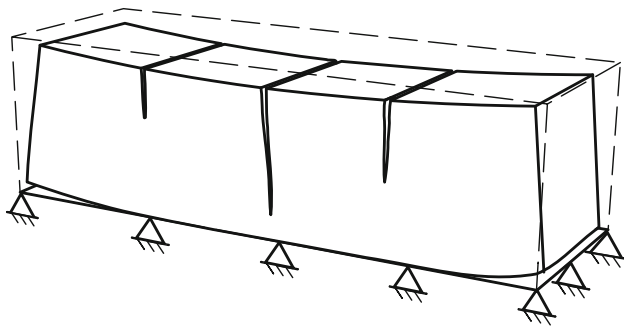


**Fig. 1** Schematic representation of desiccation cracks inspired by the experimental results in [11]. The *dashed line* stands the undeformed configuration (initial state) whereas the *solid line* shows the deformed configuration during drying. The lower restraints are distributed and unilateral. Multiple cracks initiate from the upper drying surface and propagate to the bottom. Furthermore, detachment from the mould can be also observed at the lower corners of the specimen

interface elements where a crack can propagate. Each interface is assigned a value of the tensile strength dependent on the current water content. Furthermore, the tensile strength is statistically distributed with a defined average and standard deviation. In this model, crack propagation is restricted to one direction, since the crack path is determined by the location of the interface elements and there are no transverse interface elements. In [19,20], the strain evolution in drying specimens is modeled using a diffusion like equation with a given shrinkage coefficient. This approach has the advantage of being very simple but limits the coupling between the strain and the pressure developed inside the specimen. The number of cracks is calculated analytically. On the other hand, spring and discrete models for crack propagation are adopted in [8]. Due to the weak coupling between the drying phenomenon and fracture, these models are used to predict failure qualitatively.

The phase-field approach to fracture, which started with the pioneering work of [21] on the variational formulation of the fracture problem and with its regularized counterpart [22], is recently gaining a lot of attention, see [23] for a review. Its main advantage is the possibility of modeling arbitrarily complicated crack patterns through the solution of partial differential equations. Phase-field models have a variational structure and do not need ad hoc criteria for topological changes in the crack pattern (branching or merging). The state of the material is characterized by the crack phase-field (or simply phase-field) with values ranging from 0 (intact material) to 1 (fully damaged material). A discrete crack is replaced by the steep variation of the phase-field from 0 to 1 with a characteristic width of the transition zone.

Phase-field modeling of fracture in porous media has been recently addressed for porous materials in [24–26], which however have only focused on the fully saturated

case. The original contribution of this work is to develop a modeling framework to deal with the coupled problem of desaturation and damage/crack evolution in porous media. In order to model the process of drying in a realistic manner, the flow of the fluid phase and the strain development are strongly coupled, through suitable balance equations already proposed in [27,28]. These governing equations for isothermal variably saturated porous media are here further coupled with the phase-field evolution equation. As will be discussed in the following, the coupling is realized through the use of the effective stress concept, as well as by expressing the fracture energy as a function of the water content. The weak form of the resulting system of equations is discretized with the standard finite element method and solved with a staggered approach. This paper is structured as follows: in Sect. 2, the governing equations of the poromechanical problem coupled with fracture are presented. In Sect. 3, the numerical treatment of the problem is illustrated. The computational model is verified by solving the benchmark problem of desaturation in a restrained column. Realistic constrained desiccation experiments are numerically simulated in Sect. 4, where the influence of the material properties and of the test setup on results is also systematically analyzed. Finally, conclusions are drawn in Sect. 5.

## 2 Mathematical formulation

A porous medium is composed of two or more phases, i.e. solid and fluid phases, with given volume fractions. In a fully saturated medium, only one fluid fills the voids of the material. On the other hand, in a partially saturated porous medium, two or more pore fluids are present, e.g. air and liquid water. In order to study the effects of water flow in a solid matrix, a macroscopic representation is used in poromechanical models and average properties such as density and bulk modulus are taken into account.

### 2.1 Balance equations of the poromechanical problem

The balance equations used to model deformation and flow in a variably saturated porous medium at the macroscopic level are derived from the isothermal  $\mathbf{u}$ - $p_w$  formulation for a three-phase porous medium (solid, gas, liquid phases) developed in the geometrically linear setting within the Hybrid Mixture Theory [27,28]. Here, the variable  $\mathbf{u}$  stands for the displacement vector whereas  $p_w$  is the liquid water pressure. In this study, the gas phase is composed of air and the gas pressure  $p_g$  is kept constant and equal to the atmospheric pressure. Furthermore, the air density is neglected (passive air-phase assumption [27]), resulting in the so called Isothermal Monospecies Approach [29].

The equilibrium equation of the porous medium, expressed in terms of total Cauchy stress tensor  $\boldsymbol{\sigma}$  and body forces reads

$$\nabla \cdot \boldsymbol{\sigma} + \rho \mathbf{g} = \mathbf{0} \quad (1)$$

where  $\mathbf{g}$  is the gravity acceleration vector and  $\rho$  represents the total density of the mixture computed using the following relation

$$\rho = \underbrace{(1-n)\rho_s}_{\rho_d} + nS_w\rho_w \quad (2)$$

with porosity  $n$ , density of the solid grains  $\rho_s$ , dry or bulk density  $\rho_d$ , liquid water degree of saturation  $S_w$  and liquid water density  $\rho_w$ .

The total Cauchy stress tensor depends on the generalized effective stress tensor  $\boldsymbol{\sigma}'$  [28,30] and the pressure  $p$  acting in the fluid as follows

$$\begin{aligned} \boldsymbol{\sigma} &= \boldsymbol{\sigma}' - \alpha p \mathbf{I} \\ p &\approx \chi_w p_w \end{aligned} \quad (3)$$

The coupling between the displacement  $\mathbf{u}$  and the liquid water pressure  $p_w$  is realized through the Biot parameter  $\alpha$ , which depends on the average bulk modulus of the solid skeleton  $K_T$  and the solid grain bulk modulus  $K_s$  through the relation for isotropic materials  $\alpha = 1 - K_T/K_s$ . In concrete  $0.4 \leq \alpha \leq 0.6$  and in soils typically  $\alpha \simeq 1$ . The parameter  $\chi_w$  stands for the contact area of the liquid water. Its value will be approximated by  $S_w$  in further calculations [31]. For a partially saturated medium, the concept of capillary pressure  $p_c$  (or matric suction) is defined at equilibrium as  $p_c = p_g - p_w$  [32]. Introducing the Monospecies Approach cited above, this equation is simplified to  $p_c = -p_{rw}$ , where  $p_{rw}$  is the water pressure relative to the atmospheric pressure. For simplicity, this variable is further called  $p_w$ .

In absence of cracking and assuming linearly elastic material behavior, the effective stress tensor can be computed from the constitutive tensor  $\mathcal{D}$  based on the elastic constants  $\lambda$  and  $G$  (Lamé parameters) and the infinitesimal strain tensor  $\boldsymbol{\varepsilon}$  computed as the symmetric part of the displacement gradient,

$$\boldsymbol{\sigma}' = \mathcal{D} : \boldsymbol{\varepsilon} \quad (4)$$

with

$$\boldsymbol{\varepsilon} = \nabla^s \mathbf{u}. \quad (5)$$

The substitution of Eqs. (2) and (3) into (1) results in

$$\nabla \cdot (\boldsymbol{\sigma}' - \alpha S_w p_w \mathbf{I}) + n S_w \rho_w \mathbf{g} + (1-n)\rho_s \mathbf{g} = \mathbf{0} \quad (6)$$

The second equation needed for the modeling of poromechanical processes is the mass balance equation of the liquid water,

$$\begin{aligned} \underbrace{\nabla \cdot (n S_w \mathbf{v}_{ws})}_{(i)} &+ \underbrace{\frac{S_w}{K_w} \frac{\partial p_w}{\partial t}}_{(ii)} + \underbrace{C_s \frac{\partial p_w}{\partial t}}_{(iii)} \\ &+ \underbrace{S_w \frac{\alpha - n}{K_s} \left( S_w + \frac{C_s}{n} p_w \right) \frac{\partial p_w}{\partial t}}_{(iv)} \\ &+ \underbrace{S_w \alpha \frac{\partial \text{tr}(\nabla^s \mathbf{u})}{\partial t}}_{(v)} = 0 \end{aligned} \quad (7)$$

with  $C_s = n \frac{\partial S_w}{\partial p_w}$  [27]. This equation contains the rate of water flow (i), where  $\mathbf{v}_{ws}$  is the relative velocity of the liquid water with respect to the solid phase, and the accumulation terms (ii–v), in which we can recognize the contribution of the compressive volumetric strain of the liquid water with bulk modulus  $K_w$  (ii), the variation of the water storage due to changes in liquid water saturation (iii), the change in volume of the solid phase due to the fluid pressure increase and to the effective stress (iv) and the change of strain with no variation of saturation (v) [27].

The liquid water flow is modeled by Darcy's law assuming isotropic material as

$$n S_w \mathbf{v}_{ws} = -k_{rw} \frac{k_i \mathbf{I}}{\mu_w} (\nabla p_w - \rho_w \mathbf{g}) \quad (8)$$

where the relative permeability is represented by  $k_{rw}$ , the intrinsic permeability of the material by  $k_i$  and the dynamic viscosity of the fluid by  $\mu_w$ . The intrinsic permeability is expressed in  $\text{m}^2$  and is related to the hydraulic conductivity  $k_w$  (expressed in  $\text{m/s}$ ) by

$$k_w = k_i \frac{\rho_w g}{\mu_w} \quad (9)$$

where  $g$  is the magnitude of  $\mathbf{g}$ .

The initial boundary value problem constituted by the equilibrium equation Eq. (6) and the mass balance equation of liquid water Eq. (7) [combined with Eqs. (4) and (8)], both valid in the domain of interest  $\Omega$ , is complemented by the following initial and boundary conditions:

$$\begin{aligned} p_w &= p_{w0} && \text{at } t = 0 \\ \mathbf{u} &= \mathbf{u}_0 && \text{at } t = 0 \\ \mathbf{u} &= \bar{\mathbf{u}} && \text{on } \Gamma_u \\ \boldsymbol{\sigma} \cdot \mathbf{n} &= \bar{\mathbf{t}} && \text{on } \Gamma_t \\ p_w &= \bar{p}_w && \text{on } \Gamma_p \\ k_{rw} \frac{k_i \mathbf{I}}{\mu_w} (-\nabla p_w + \rho_w \mathbf{g}) \cdot \mathbf{n} &= \bar{q} && \text{on } \Gamma_q \end{aligned} \quad (10)$$

where  $\mathbf{n}$  is the outward unit normal vector to the surface of the porous medium,  $\bar{\mathbf{t}}$  is the imposed traction vector and  $\bar{q}$  is the imposed liquid water flux.  $\Gamma_u$  and  $\Gamma_t$  are respectively the Dirichlet and Neumann portions of the boundary  $\Gamma = \partial\Omega$  associated to the displacement variable  $\mathbf{u}$ , whereas  $\Gamma_p$  and  $\Gamma_q$  are respectively the Dirichlet and Neumann portions of  $\Gamma$  associated to  $p_w$ . It is  $\Gamma_u \cup \Gamma_t = \Gamma_p \cup \Gamma_q = \Gamma$  and  $\Gamma_u \cap \Gamma_t = \Gamma_p \cap \Gamma_q = \emptyset$ . We further assume consistency of the initial and boundary conditions, i.e.  $\bar{\mathbf{u}} = \mathbf{u}_0$  at  $t = 0$  on  $\Gamma_u$  and  $\bar{p}_w = p_{w0}$  at  $t = 0$  on  $\Gamma_p$ .

## 2.2 Additional constitutive relations

To complete the description of the multiphase model, some additional constitutive equations must be specified. In a partially saturated medium, the degree of saturation  $S_w$  and the relative permeability  $k_{rw}$  are experimentally-based functions of the capillary pressure or the water pressure head  $\varphi = \frac{p_c}{\rho_w g} = \frac{-p_w}{\rho_w g}$ . Commonly used functions are given by the van Genuchten model [33],

$$S_w = (1 - S_r) \cdot S_e + S_r \quad (11)$$

$$S_e = (1 + (\alpha_{vG} \cdot \varphi)^{n_{vG}})^{-m_{vG}} \quad (12)$$

$$k_{rw} = \sqrt{S_e} \left[ 1 - \left( 1 - S_e^{1/m_{vG}} \right)^{m_{vG}} \right]^2 \quad (13)$$

where  $S_e$  is the effective saturation and  $S_r$  is the residual saturation, which can be determined experimentally on a very dry soil. The parameters  $\alpha_{vG}$  and  $n_{vG}$  represent the air entry value and the rate of drying, respectively, and are obtained from the experimental solid water retention curve. The parameter  $m_{vG}$  is computed using the relation  $m_{vG} = 1 - 1/n_{vG}$  as presented in [33].

The parameters used in each numerical test are specified in the respective example. In all computations, the bulk modulus of the solid grain and the liquid water as well as the dynamic viscosity of the liquid water are assumed as constant material parameters as follows:  $K_s = \lambda + 2/3 G$ ,  $K_w = 2.2$  GPa and  $\mu_w = 0.001$  Pas.

## 2.3 Phase-field modeling approach to fracture and coupling to the poromechanical model

The numerical modeling of cracking is performed within the phase-field framework, which is based on a regularization of Griffith's theory of fracture [22]. The governing equations of the classical brittle mechanical fracture problem stem from the minimization of the following energy functional

$$E_\ell(\mathbf{u}, d) = \int_\Omega [g(d)\Psi^+(\boldsymbol{\varepsilon}) + \Psi^-(\boldsymbol{\varepsilon})] d\Omega$$

$$+ \mathcal{G}_c \int_\Omega \left( \frac{1}{2\ell} d^2 + \frac{\ell}{2} |\nabla d|^2 \right) d\Omega. \quad (14)$$

In this equation,  $d$  is the crack phase-field that characterizes the state of the material with values ranging from 0 (intact material) to 1 (fully damaged material),  $\ell$  is the crack length scale parameter that represents the width of the transition zone between cracked and intact states,  $\mathcal{G}_c$  has been given different names in the literature: fracture resistance related to the fracture toughness [34], fracture toughness [23], critical energy release rate [24] and fracture energy [26, 35]. In this paper we chose to indicate it as fracture energy. The degradation function  $g(d)$  is defined as

$$g(d) = [(1 - d)^2 + \eta] \quad (15)$$

where  $\eta$  is a very small residual stiffness used to keep numerical stability in fully cracked conditions.

The elastic energy density  $\Psi$  is split into positive or tensile  $\Psi^+$  and negative or compressive  $\Psi^-$  contributions

$$\Psi(\boldsymbol{\varepsilon}) = \Psi^+(\boldsymbol{\varepsilon}) + \Psi^-(\boldsymbol{\varepsilon}). \quad (16)$$

There are different splits proposed in the literature, such as the spectral decomposition [36], the combined cleavage-deviatoric split [37] and the volumetric-deviatoric split [38]. In this work, we choose the split proposed by Amor et al. [38], i.e.

$$\begin{aligned} \Psi^+(\boldsymbol{\varepsilon}) &= \frac{1}{2} \left( \lambda + \frac{2}{3} G \right) \langle \text{tr}(\boldsymbol{\varepsilon}) \rangle_+^2 + G(\boldsymbol{\varepsilon}^{\text{dev}} : \boldsymbol{\varepsilon}^{\text{dev}}) \\ \Psi^-(\boldsymbol{\varepsilon}) &= \frac{1}{2} \left( \lambda + \frac{2}{3} G \right) \langle \text{tr}(\boldsymbol{\varepsilon}) \rangle_-^2 \end{aligned} \quad (17)$$

where  $\langle \text{tr}(\boldsymbol{\varepsilon}) \rangle_\pm = \frac{1}{2} (\text{tr}(\boldsymbol{\varepsilon}) \pm |\text{tr}(\boldsymbol{\varepsilon})|)$  and  $\boldsymbol{\varepsilon}^{\text{dev}} = \boldsymbol{\varepsilon} - \frac{1}{3} \text{tr}(\boldsymbol{\varepsilon})$  is the deviatoric strain tensor. Only the positive part of the energy is degraded. This split is meant to prevent cracking under compression and to enforce crack face contact in phase-field models. However it is known not to resolve all the connected issues. The development of an optimal split is still an open issue in the literature.

The degradation function realizes the coupling between the phase-field evolution and the mechanical problem. In the present case, where the standard mechanical problem is replaced by a poromechanical formulation, the *first source of coupling* between the poromechanical problem and the fracture problem is obtained through the concept of effective stress. The generalized effective stress is expressed as:

$$\boldsymbol{\sigma}' = g(d) \boldsymbol{\sigma}'^+ + \boldsymbol{\sigma}'^- \quad (18)$$

where

$$\begin{aligned}\sigma'^+ &= \frac{\partial \Psi^+(\boldsymbol{\varepsilon})}{\partial \boldsymbol{\varepsilon}} = \left( \lambda + \frac{2}{3} G \right) \langle \text{tr}(\boldsymbol{\varepsilon}) \rangle_+ \mathbf{I} + 2G \boldsymbol{\varepsilon}^{dev} \\ \sigma'^- &= \frac{\partial \Psi^-(\boldsymbol{\varepsilon})}{\partial \boldsymbol{\varepsilon}} = \left( \lambda + \frac{2}{3} G \right) \langle \text{tr}(\boldsymbol{\varepsilon}) \rangle_- \mathbf{I}\end{aligned}\quad (19)$$

The constitutive tensor of the solid skeleton is computed corresponding to the stress split,

$$\mathcal{D} = \mathcal{D}^+ + \mathcal{D}^- \quad (20)$$

with positive and negative parts given by:

$$\begin{aligned}\mathcal{D}^+ &= \frac{\partial \sigma'^+}{\partial \boldsymbol{\varepsilon}} \\ \mathcal{D}^- &= \frac{\partial \sigma'^-}{\partial \boldsymbol{\varepsilon}}\end{aligned}\quad (21)$$

The necessary condition for minimization of Eq. (14) with respect to  $d$  leads to the phase-field evolution equation [36, 39]

$$\frac{\mathcal{G}_c}{\ell} [d - \ell^2 \nabla d] - 2(1 - d)\mathcal{H} = 0 \quad (22)$$

where  $\mathcal{H} = \max_{\tau \in [0, t]} \Psi^+(\nabla^s \mathbf{u}, \tau)$  is the maximum energy within the loading history up to the current instant  $t$ . The introduction of  $\mathcal{H}$  is used to enforce the irreversibility of the phase-field evolution equation within a staggered solution scheme [36].

The fracture energy can be determined experimentally by direct and indirect tests, e.g. Brazilian test [40] and compact tension tests [2]. For clayey materials, the value of  $\mathcal{G}_c$  is not uniquely defined in the literature. It is found that it can be a function of the water content of the porous medium [4, 5]. Based on the so-called homogeneous solution of the phase-field problem, the fracture energy is related to the tensile strength  $\sigma_t$ , Young's modulus  $E$  and crack length scale  $\ell$  as [41]

$$\sigma_t = \frac{9}{16} \sqrt{\frac{\mathcal{G}_c E}{6\ell}}. \quad (23)$$

In this work, we follow the approach to compute the fracture energy by keeping the length scale parameter constant and expressing  $\sigma_t$  and  $E$  as functions of the water content  $w = nS_w \rho_w / \rho_d \times 100$ . For this reason,  $\mathcal{G}_c$  also becomes a function of the water content as follows

$$\mathcal{G}_c(w, \ell) = \left( \frac{16}{9} \right)^2 \sigma_t(w)^2 \frac{6\ell}{E(w)}. \quad (24)$$

This is thus the *second source of coupling* between the poromechanical and the fracture problems. From this equation, and with the choice of the functions  $\sigma_t(w)$  and  $E(w)$  that will be illustrated later, the fracture energy decreases with drying and cracking becomes more likely to occur. This behavior is in agreement with experiments relating the water content and the fracture energy in specimens with variable water content [2].

Equations (6), (7) and (22), together with the constitutive Eqs. (8), (11)–(13) and (19) define the coupled  $\mathbf{u}$ - $p_w$ - $d$  problem in strong form. Note that in this first sample modeling approach, we are not considering the development of the phase-field on the hydraulic properties and especially on the permeability. This rather crude assumption will be removed in further ongoing work.

### 3 Numerical solution

In the following, the numerical treatment of the governing equations is briefly presented. The discretization of the equations with respect to space and time followed by the linearization of the coupled system of equations is shown. Furthermore, the algorithmic procedure is discussed.

#### 3.1 Discretized formulation

The spatial discretization of the  $\mathbf{u}$ - $p_w$ - $d$  problem of Eqs. (6), (7) and (22) is performed using the weighted residual method and the standard Bubnov-Galerkin approach. For time discretization, the backward Euler method is applied. Due to the nonlinearity of the problem, the discretized equations are linearized with the Newton-Raphson method. A staggered scheme is adopted in this work for the solution of the coupled  $\mathbf{u}$ - $p_w$ - $d$  discrete system, where first the crack evolution equation is solved, followed by the monolithic solution of the  $\mathbf{u}$ - $p_w$  discrete equations. For the  $\mathbf{u}$ - $d$  problem, staggered (often called alternate minimization) schemes are known to be less efficient but more robust than monolithic schemes. In particular, staggered schemes always converge, although at the cost of a number of staggered iterations which is heavily influenced by the time step size and which can be very large, see the detailed discussion in [42].

In particular, after spatial and time discretization, the following non-symmetric, non-linear and coupled discretized  $\mathbf{u}$ - $p_w$  algebraic system of equations is obtained

$$\begin{aligned}\mathbf{F}(\mathbf{U}) &= \begin{bmatrix} K_e & Q \\ -Q^T & S + \Delta t H \end{bmatrix}_{n+1} \mathbf{U}_{n+1} + \\ &\begin{bmatrix} 0 & 0 \\ Q^T & -S \end{bmatrix}_{n+1} \mathbf{U}_n + \begin{bmatrix} f^{\mathbf{u}} \\ \Delta t f^p \end{bmatrix}_n, \quad \mathbf{U} = \begin{bmatrix} \mathbf{u} \\ p_w \end{bmatrix}\end{aligned}\quad (25)$$



where the subscripts  $n$  and  $n + 1$  denote respectively the previous and the current time steps,  $t_n$  and  $t_{n+1}$ . In Eq. (25):

$$\begin{aligned} K_e &= (\nabla \phi^u, [(1-d)^2 + \eta] \cdot \mathcal{D}^+ \nabla \phi^u)_{\Omega} + (\nabla \phi^u, \mathcal{D}^- \nabla \phi^u)_{\Omega} \\ Q &= -(\nabla \phi^u, \alpha S_w \phi^p \mathbf{I})_{\Omega} \\ f^u &= -(\phi^u, n S_w \rho_w \mathbf{g})_{\Omega} - (\phi^u, (1-n) \rho_d \mathbf{g})_{\Omega} - (\phi^u, \bar{t})_{\Gamma} \\ H &= (\nabla \phi^p, k_w \nabla \phi^p)_{\Omega} \\ S &= \left( \phi^p, \left( n \frac{S_w}{K_w} + C_s + S_w \frac{\alpha - n}{K_s} \left( S_w + \frac{C_s}{n} p_w \right) \right) \phi^p \right)_{\Omega} \\ f^p &= -(\nabla \phi^p, k_w S_w \rho_w \mathbf{g})_{\Omega} + (\phi^p, \bar{q})_{\Gamma}. \end{aligned}$$

where  $\phi^u$  and  $\phi^p$  are the shape functions for the discretization of  $\mathbf{u}$  and  $p_w$ , respectively. The bilinear functional integrated over the domain  $\Omega$  and the linear functional integrated over the boundary  $\Gamma$  are denoted by  $(\cdot, \cdot)_{\Omega}$  and  $(\cdot)_{\Gamma}$ , respectively. The shape functions  $\phi^u$  and  $\phi^p$  are chosen in such a way to satisfy the Ladyzhenskaya–Babuška–Brezzi condition for the locally undrained case. In this work, we adopt quadratic functions for the displacements and linear functions for the pore pressure (Taylor–Hood pair) [27, 28, 43].

The equations are linearized to be solved with the Newton–Raphson method, i.e.

$$\mathbf{F}'(\mathbf{U}_{n+1}^i, \delta \mathbf{U}_{n+1}^{i+1}) = -\mathbf{F}(\mathbf{U}_{n+1}^i) \quad (26)$$

where the superscript  $i$  refers to the  $i$ th Newton–Raphson iteration. The Jacobian matrix  $\mathbf{F}'$  provided by the linearization with respect to  $\mathbf{u}$  and  $p_w$  is given by

$$\mathbf{F}'(\mathbf{U}^i, \delta \mathbf{U}^{i+1}) = \begin{bmatrix} \frac{\partial K_e}{\partial \mathbf{u}} & \frac{\partial}{\partial p_w} (Q + f^u + K_e) \\ -\frac{\partial Q^T}{\partial \mathbf{u}} & \frac{\partial}{\partial p_w} (\Delta t H - Q^T + \Delta t f^p) \end{bmatrix}_{n+1}^i \delta \mathbf{U}_{n+1}^{i+1}. \quad (27)$$

Finally, the solution vector is updated as follows

$$\mathbf{U}_{n+1}^{i+1} = \mathbf{U}_{n+1}^i + \delta \mathbf{U}_{n+1}^{i+1}. \quad (28)$$

The discretized weak form of the phase-field evolution equation is given by

$$\begin{aligned} \left( \phi^d, \frac{\mathcal{G}_c}{\ell} \phi^d d \right)_{\Omega} - \left( \nabla \phi^d, \frac{\mathcal{G}_c}{\ell} (-\ell^2 \nabla \phi^d d) \right)_{\Omega} \\ - \left( \phi^d, 2(1 - \phi^d d) \mathcal{H} \right)_{\Omega} = 0 \end{aligned} \quad (29)$$

This equation does not require further numerical treatment. The shape functions used to discretize the phase-field variable,  $\phi^d$ , are quadratic as the displacement shape functions.

The discretized system is implemented in the finite element library `deal.II` [44]. As mentioned earlier, the solution of the complete system follows a staggered scheme

[36], as summarized in Algorithm 1. All required parameters such as the initial and boundary values are initialized at  $t = 0$ . Furthermore, the stored elastic energy is set to zero. First, the crack-field evolution equation is solved at the current time  $t_{n+1}$ . Then, the phase-field solution vector is frozen and inserted in the poromechanical equations. The values of displacements and water pressure are computed at  $t_{n+1}$ , the corresponding solution vector  $\mathbf{U}$  is frozen and the stored elastic energy is calculated/updated at each integration point. The history variable is updated if the current computed energy is larger than the previously computed energy, i.e. if the energy is increasing. This is important to ensure the irreversibility of the crack-field variable. The history variable is inserted in the crack evolution equation and a new time step can be applied. It is important to note that the value of the water content after the solution of the poromechanical system is also updated at each integration point so that the fracture energy can assume the correct value according to Eq. (24).

**Initialization** ( $t = t_0 = 0$ ):  $\bar{\mathbf{u}}, \bar{\mathbf{t}}, \bar{p}, \bar{q}, \bar{d}, \mathcal{H} = 0$ ;

**for**  $n = 0 : N-1$  **do**

    compute  $\Psi^+(t = t_{n+1})$

**if**  $\Psi^+ > \mathcal{H}_n$  **then**

$\mathcal{H}_{n+1} \leftarrow \Psi^+(t = t_{n+1})$ ;

**else**

$\mathcal{H}_{n+1} = \mathcal{H}_n$ ;

**end**

    solve  $d_{n+1}(\mathcal{H}_{n+1})$ ;

    solve  $\mathbf{u}-p_w := \mathbf{U}_{n+1}(d_{n+1})$ ;

**end**

**Algorithm 1:** Algorithmic solution procedure for the  $\mathbf{u}-p_w-d$  system

## 3.2 Verification of the numerical solution

The discretized set of linearized equations from the previous section is applied to study different numerical setups of variably saturated samples. The first two examples aim at validating the  $\mathbf{u}-p_w$  model and at verifying the capability of the  $\mathbf{u}-p_w-d$  equations to simulate the crack development due to desaturation. In all examples, we consider the gravity  $g = 9.81 \text{ m/s}^2$ . The fluid phase is liquid water with density  $\rho_w = 1000 \text{ kg/m}^3$ . The time increment is set to  $\Delta t = 1 \text{ s}$ .

### 3.2.1 Desaturation of a column

This example is based on the experiment performed by Liakopoulos [45] concerning outflow of liquid water from a sand column due to gravity force. First, before starting the experiment ( $t < 0$ ), liquid water was continuously added from the top of a column of perspex with height  $h = 1 \text{ m}$  filled with Del Monte sand and was allowed to drain freely at

the bottom through a filter. When uniform flow was observed, the inflow of water was stopped ( $t = 0$ ). The experiment revealed desaturation of the soil column from the top due to the action of the gravity force. A more detailed explanation regarding the test can be found in [46, 47]. In order to model the drainage process, the water pressure is kept constant at the bottom of the column and is equal to the seepage pressure ( $p_w = 0$ ). The boundary conditions are shown in Fig. 2a. The solid grain and liquid water are considered incompressible during the numerical simulation.

The constitutive equations for the water saturation and the relative permeability as presented in [46] are

$$\begin{aligned} S_w &= 1 - 1.9722 \times 10^{-11} p_c^{2.4279} \\ k_{rw} &= 1 - 2.207(1 - S_w)^{0.9529}. \end{aligned} \quad (30)$$

The material parameters used during the numerical test can be found in Table 1.

The water loss from the bottom induces capillary pressure development along the column starting from the top, which, in turn, leads to partially saturated conditions and therefore to changes in the relative permeability and moisture con-

tent. The suction together with the action of the gravity leads to the shrinkage of the column. Since the vertical displacements along the column are free, the column can deform vertically.

The numerical results of  $\mathbf{u}$ ,  $p_w$  and  $S_w$  are compared with those of the benchmark results [48] from the Comes-Geo finite element code [28, 46, 47, 49] and show good agreement, see Fig. 3. The plotted displacements are related exclusively to the time dependent process, i.e. the displacement due to consolidation of the specimen is subtracted. A slightly different response of the vertical displacement is observed due to the use of the Taylor-Hood pair, while the results in [46–48] were obtained with bi-quadratic elements for the nodal displacements and pore pressures.

### 3.2.2 Desaturation of a restrained column

In the previous example, the column deforms freely in the vertical direction, allowing the elastic energy to be fully released and, consequently, avoiding cracking. In order to verify the capability of the  $\mathbf{u}$ - $p_w$ - $d$  model to describe crack development, the nodes of the upper surface of the previous example are now restrained, Fig. 2b. The other boundary conditions remain as in the previous example.

In the model, the water loss induces capillary pressures from the upper surface and, together with the mechanical constraint which prevents the settlement of the column, the formation of a positive vertical stress distribution in the same zone of the column as shown in Fig. 4a at an early time step,  $t = 3$  s. Cracking is expected to occur in the tension zone.

Since the fracture properties of the material are not available in the literature, test values have been chosen for  $\mathcal{G}_c = 0.5$  N/m and  $\ell = 0.01$  m, the latter corresponding to 1% of the height of the column. The mesh is refined only along the vertical direction with element size  $\ell/2$ . With these parameters, localization of the crack-field variable is predicted by the numerical model at the top of the column. Figure 4b shows the phase-field distribution in the upper part of the column (vertical coordinate between 0.9 h and h). It can be observed that the thickness of the localization zone is consistent with the chosen crack length parameter.

The corresponding degree of saturation in the cracked region is  $S_w \approx 1$ . The susceptibility of crack formation when  $S_w \approx 1$  is in agreement with Péron's observations [4], who classified three domains for the water saturation degree. The first domain corresponds to full saturation, where cracking is unlikely to occur. With the increase of suction and, consequently, changes in saturation,  $S_w \approx 1$ , the medium is close to the air entry conditions and more susceptible to cracking. The third saturation domain corresponds

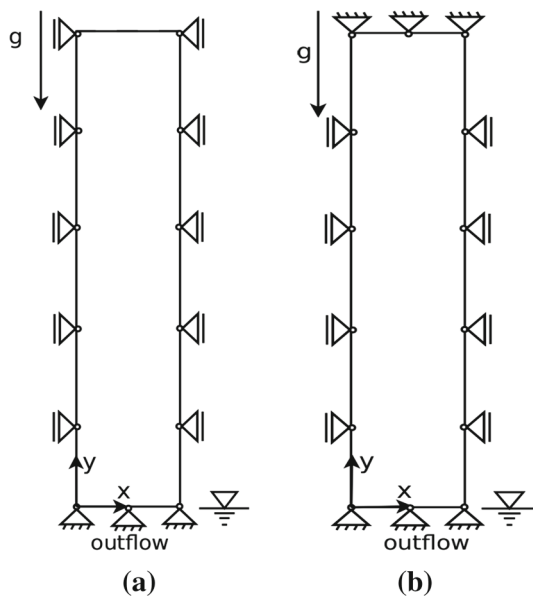


**Fig. 2** Boundary conditions for **a** desaturation and **b** restrained desaturation problems. The water level indicates that seepage pressure is imposed. The mechanical boundary conditions are shown schematically. Impervious and traction free boundary conditions are imposed over the remaining boundaries. The column is 1 m high and 0.1 m wide

**Table 1** Parameters used in the modeling of a column subject to desaturation

n	$\rho_s$	E	$\nu$	$k_i$
0.2975	2000 kg/m <sup>3</sup>	1.3 MPa	0.4	$4.5 \times 10^{-13}$ m <sup>2</sup>

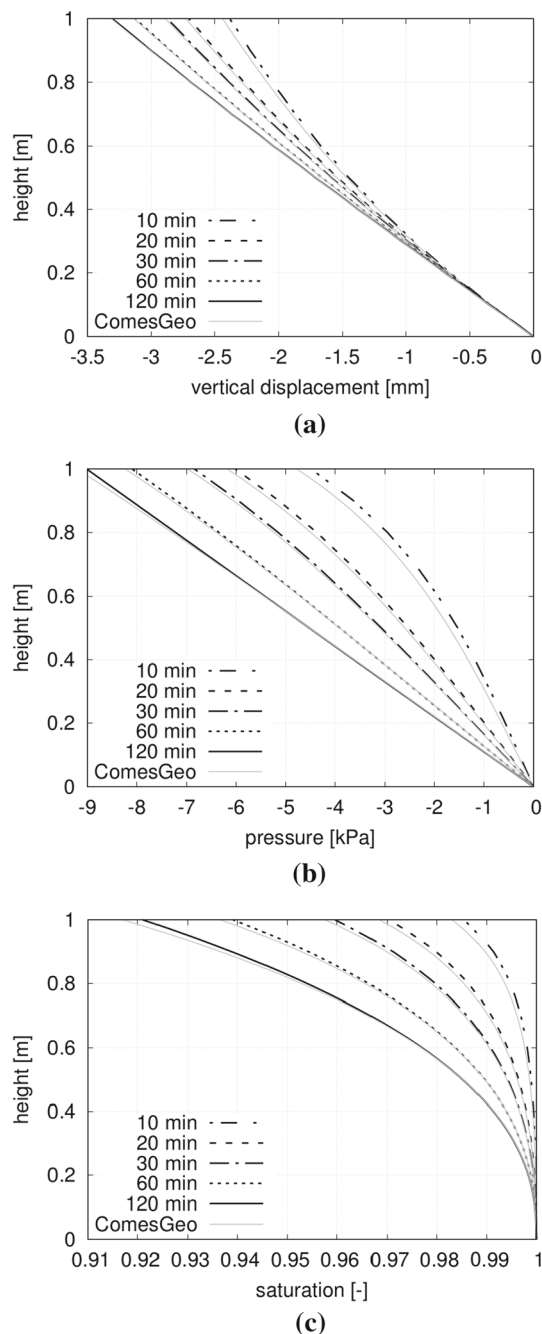


**Fig. 3** **a** Vertical displacement of the top edge, **b** liquid water pressure distribution and **c** water saturation degree along the column subject to desaturation and comparison with results from ComesGeo [47–49]

to lower water saturation degrees at which the air phase is connected.

#### 4 Constrained desiccation test

In the following, a numerical model based on an experimental constrained desiccation test is presented. A reference

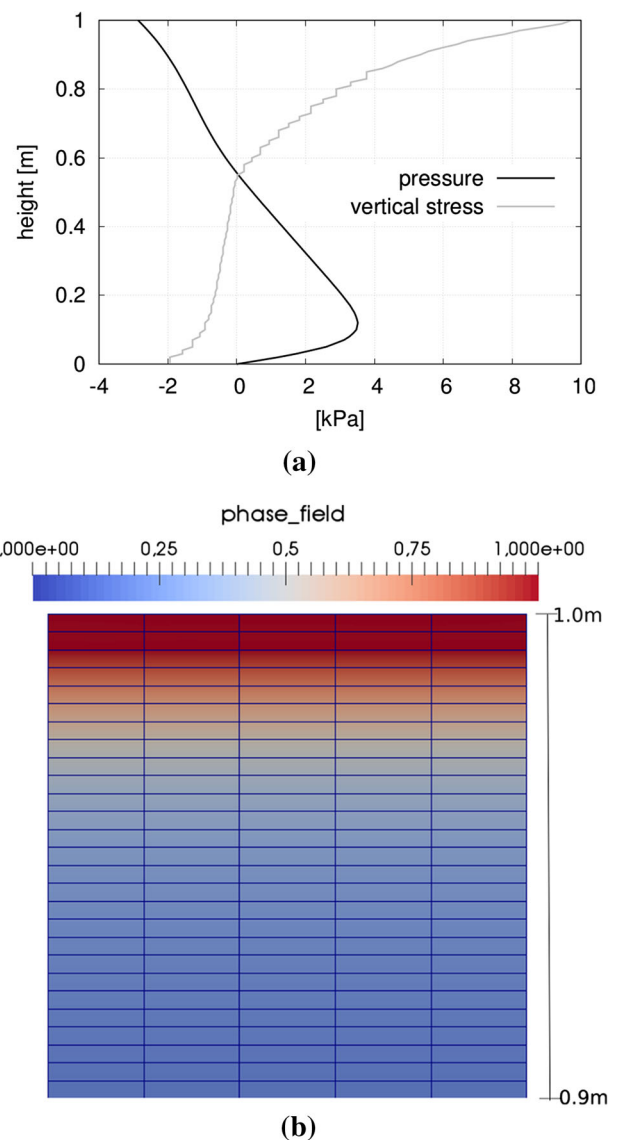


**Fig. 4** Desaturation of a restrained column with test parameters  $\mathcal{G}_c = 0.5 \text{ N/m}$  and  $\ell = 0.01 \text{ m}$ . **a** Vertical stress and water pressure distributions at early stage  $t = 3 \text{ s}$  showing the positive and negative stress distribution along the column. **b** Phase-field evolution along the upper part of the restrained column with vertical coordinate between 0.9 and 1 m at  $t \approx 150 \text{ s}$

model is computed and results are analyzed in detail. Additionally, we investigate the influence of the fracture energy, the mechanical restraint, the drying flux and the intrinsic permeability on the numerical results.

#### 4.1 Description of the test and input parameters

A constrained desiccation test is performed in order to show the capability of the model to describe the formation of multiple cracks during drying. The experimental tests from Péron [4] and Stirling [5, 18] are utilized as



qualitative reference in the following numerical tests. Both authors consider clayey materials subjected to drying. Péron focused his study on the desiccation of rectangular specimens restrained at the bottom while Stirling's specimen is inserted into a semi-cylindrical mould and left to dry. In Stirling's tests, there is no access to the sides of the specimen. The upper surface of the specimen is visible and the results are related to the top view. However, his work provides more detailed information regarding the hydraulic and mechanical properties of the material, that are necessary in our framework. For this reason, we utilize his data in the next numerical tests. Additionally, some observations provided by Péron are taken into account in the description of the behavior of constrained drying specimens.

Stirling's experimental setup consists of a steel mould which is first sandblasted. After the mould has a fixed sand line, it is filled with clay so that higher friction is created corresponding to a mechanical restraint. The clay is then compacted with a hammer for the purposes of homogenization and increase of the dry density. The density obtained by the author varies in the range of 1600–1650 kg/m<sup>3</sup>.

The desiccation process starts with the initially water saturated compacted material. Drying is induced due to increase of temperature around the specimen. After 1 h, a crack has already initiated on the surface of the specimen, propagating further on the upper surface and then vertically to the bottom of the mould. After 17 h from the beginning of the test, the maximum degree of shrinkage is achieved. No remarkable changes are observable in the next hours. The complete test takes 144 h. Stirling observed one to two cracks that fully propagate through the specimen and several secondary cracks, i.e. cracks that do not propagate until the bottom. The differences in the crack propagation are related to the velocity of drying. No exact specifications regarding the crack onset time are reported.

In the numerical test, a two-dimensional half model of the specimen's longitudinal cross section is studied. This test is not aiming at quantitatively reproducing the experimental results but just at verifying if a qualitative agreement can be obtained. The model dimensions are  $0.285 \times 0.051 \text{ m}^2$ . The flux  $\bar{q}$  is applied on the free drying surfaces of the specimen, while the bottom of the specimen is mechanically constrained as shown in Fig. 5. The value of the drying flux is chosen according to the discharge rates presented in [5]. The discharge rate is determined experimentally by the author. The material parameters can be found in Table 2. Furthermore the compressibility (bulk modulus) of the solid grains and the liquid water are taken into account.

Finally, it is important to point out that the stiffness and the strength of the material increase during drying. Stirling proposed two functions relating the Young's modulus  $E$  and

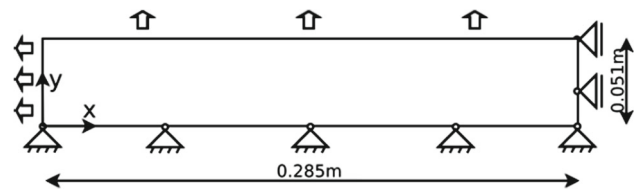


**Fig. 5** Constrained experimental based desiccation test. The model indicates the half-geometry used and mechanical boundary conditions. The applied drying flux  $\bar{q}$  is represented by the arrows

the tensile strength  $\sigma_t$  with the water content  $w$ , as follows

$$E = 1770 \exp(-0.297w) \text{ MPa} \quad (31)$$

$$\sigma_t = 228.85 \exp(-0.14w) \text{ kPa} \quad (32)$$

These functions are used to compute the fracture energy of the material through Eq. (24). As indicated in Table 2, the length scale parameter is set to  $\ell = 0.002 \text{ m}$ . This value leads to a reasonable fracture energy ( $\mathcal{G}_c(w = 0) = 1.12 \text{ N/m}$  and  $\mathcal{G}_c(w = 100) = 1.71 \text{ N/m}$ ) as found in the literature for clayey materials [1, 4]. As a result of a preliminary convergence study, we set the element size to  $h = \ell/2$  and adopt  $\Delta t = 1 \text{ s}$ . Since the time increment is very small, the phase-field evolution equation is solved explicitly, i.e. no staggered iterations are carried out. In order to check the accuracy of the results, some tests were run with 10 staggered iterations and results are reported in “Appendix A”. The residual stiffness is set to  $\eta = 10^{-6}$ . The end time of the simulation is  $t = 120 \text{ min}$ .

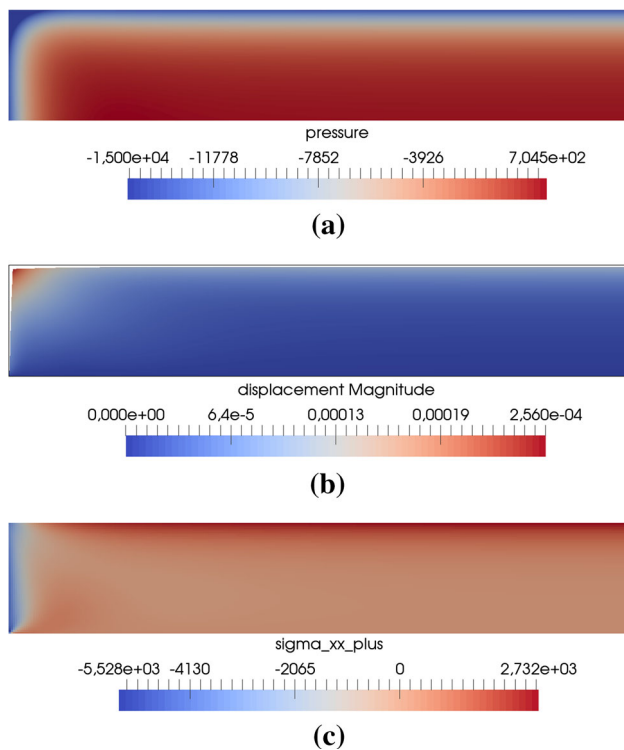
As observed in the previous examples, gravity can be the unique driving load leading to development of capillary pressure along the specimen when a seepage pressure is imposed as a strong boundary condition. Additionally, non-homogeneous Neumann natural boundary conditions can be applied. The applied flux can be constant or a function of time. In our numerical tests, we apply a constant drying flux on the free surfaces of the specimen (see Fig. 5; Table 2).

## 4.2 Reference test

When the drying process starts, suction develops on the free surfaces of the specimen. First, the specimen shrinks vertically followed by lateral shrinkage. The extraction of the water leads to increase of the suction that consequently leads to increase of the horizontal stresses along the specimen. In an early phase the horizontal stress is uniform along the upper drying surface of the specimen. At the extremity of the specimen, where the drying fluxes from the side and upper surfaces overlap, the horizontal stress is negative. A first qualitative study is shown in Fig. 6, where the pressure, displacement magnitude and horizontal stress fields are plotted. The negative pressure layer around the specimen (blue

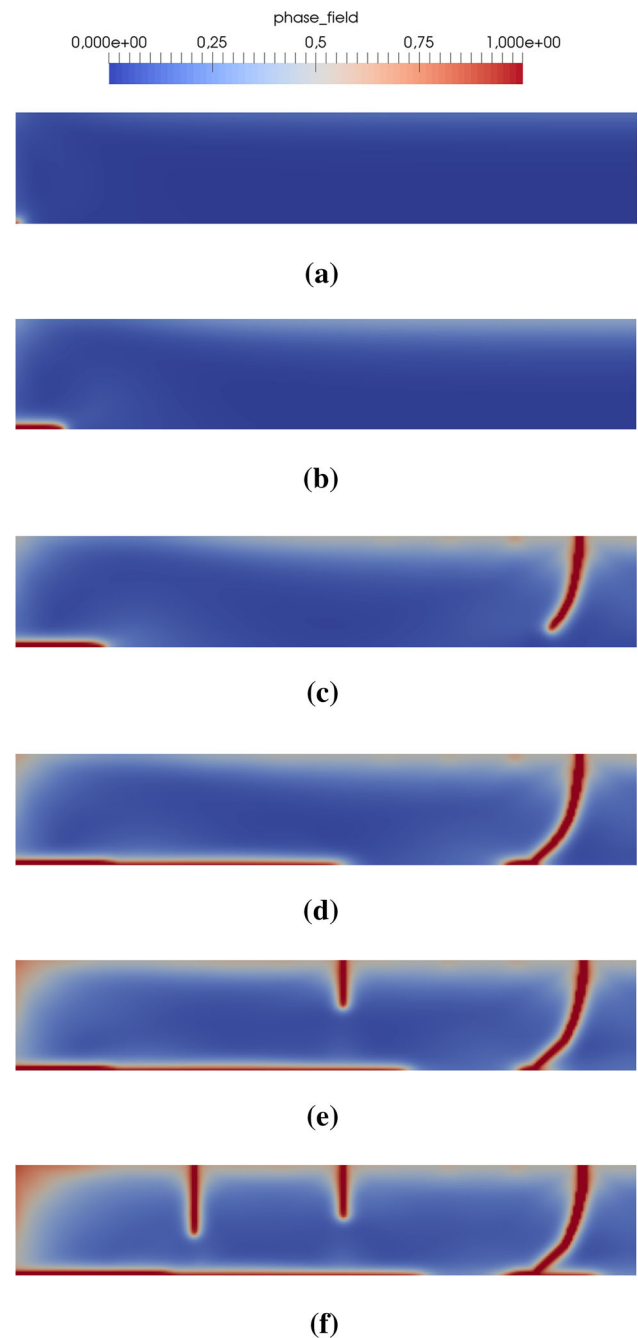
**Table 2** Parameters utilized in the modeling of the constrained desiccation test

$n$	$\rho_d$	$k_i$	$\alpha_{vG}$	$S_r$	$n_{vG}$	$m_{vG}$	$\bar{q}$	$\ell$
0.41	1650 kg/m <sup>3</sup>	10 <sup>-15</sup> m <sup>2</sup>	0.028 m <sup>-1</sup>	0.15	1.3	1-1/ $n_{vG}$	$6 \times 10^{-7}$ m/s	0.002 m

**Fig. 6** **a** Liquid water pressure in Pa, **b** displacement magnitude in  $m$  plotted on the deformed configuration and scaled with factor 10 and **c** horizontal stress fields in Pa at  $t = 5$  min in the early stage for general evaluation of the behavior of the specimen during drying and before cracking

region in Fig. 6a) corresponds to higher suction values due to the applied drying flux in this region. The suction layer will extend to the interior of the specimen with time. The computation of the saturation degree along the extending drying layer reveals  $S_w \approx 1$ , which from experimental observations is known to be a favorable condition for cracking [4], see also end of Sect. 3. We observe first vertical then lateral shrinkage in the specimen based on its deformed configuration in Fig. 6b. The shrinkage is a result of the gravity action and applied drying flux. The horizontal stress field has a positive uniform distribution on the upper surface of the specimen except for the very left edge, Fig. 6c. The values close to the surface are higher than in the interior of the specimen. Due to the tensile nature of these stresses, crack in mode I is expected to occur, starting from the upper drying surface. This behavior has been observed in diverse experiments related to desiccation cracks in soils and also plain cement.

The uniform stress distribution corresponds to an uniform phase-field distribution, Fig. 7a, b. The first localization zones

**Fig. 7** Phase-field evolution in the reference specimen subject to drying flux  $\bar{q} = 6 \times 10^{-7}$  m/s. At **a**  $t = 15$  min, the phase-field distribution is uniform on the surface and the crack at the corner initiated. Further propagation of the crack at the corner is observed at **b**  $t = 30$  min. Drying crack onset is registered at  $t \approx 41$  min. Specimen at **c** 45 min, **d** 60 min, **e** 90 min and **f** 120 min

of the crack field at the drying surface occur after 41 min from the test start, Fig. 7c. With further drying, the suction and the horizontal stress increase at the upper region and drive propagation of the upper crack downwards, Fig. 7d. After full propagation of the upper crack, the crack at the corner propagates further and the specimen starts detaching from the bottom. At  $t = 85$  min, a second crack is observed in the medium, Fig. 7e, followed by a third one that initiates 16 min later as shown in Fig. 7f. Also, the crack at the bottom propagates further and the sample is almost fully detached from the bottom. The full detachment would lead to the release of the constraints, so that further desiccation occurs in free conditions and no further cracking would be observed.

It is interesting to understand the variation of quantities such as water pressure, degree of saturation and fracture energy during the test. The water pressure distribution along the specimen is shown in Fig. 8 for different time steps. The suction layer expands gradually to the inner core of the specimen. After 15 min from the start of the test, the water pressure is negative everywhere and decreases continuously until the end of the test at 120 min. The distribution of the saturation degree is given in Fig. 9. At the beginning of the test, the specimen is fully saturated,  $S_w = 1$ . Due to the increase of suction in the medium as shown previously, the saturation degree decreases. At 15 min of test,  $S_w \approx 0.99$  in the outer layer of the specimen (except at the upper left corner), Fig. 9a. It is possible to recognize that the saturation degree in the inner part of the specimen is much higher than on the outer surface. This is related to the higher values of suction along the surface. Subsequently, the saturation degree decreases gradually, Fig. 9b–e, to a value of about 0.897 at the upper layer as shown in Fig. 9f.

As previously mentioned, the fracture energy is a function of the water content in the body, which is computed from  $S_w$ . At the beginning of the test, the maximum value of the fracture energy is observed with  $\mathcal{G}_c = 1.712$  N/m. This value decreases with drying reaching the minimum of  $\mathcal{G}_c = 1.639$  N/m excluding the corner region of the specimen. At the left extremity of the specimen,  $\mathcal{G}_c = 1.417$  N/m. The results are shown in Fig. 10.

### 4.3 Sensitivity of the numerical solution

In the following, we present the results of additional numerical simulations, which aim at evaluating how the choice of fracture energy, dry density, permeability and boundary conditions affects the results.

#### 4.3.1 Influence of the fracture energy

As shown in Eq. (23), the length scale parameter is related to the material properties (fracture energy, tensile strength

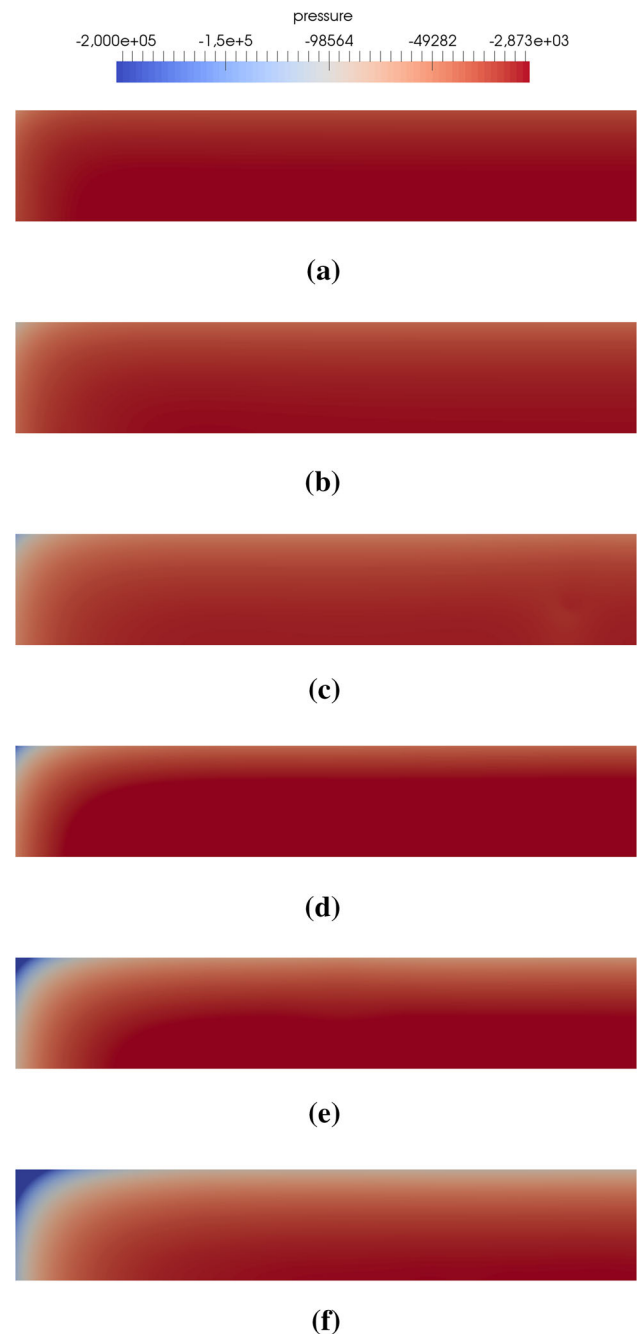


**Fig. 8** a Water pressure (Pa) distribution in the reference specimen subject to drying flux  $\bar{q} = 6 \times 10^{-7}$  m/s at  $t = 15$  min, **b** 30 min, **c** 45 min, **d** 60 min, **e** 90 min and **f** 120 min

and elastic modulus). As we decided to keep  $\ell$  constant and consider  $\sigma_t$  and  $E$  as functions of  $w$  only, the fracture energy turns out to increase linearly with  $\ell$  (Eq. 24). Furthermore, the width of the regularization zone proportionally increases with  $\ell$ .

We now show the results of the constrained desiccation test when the length scale parameter is increased to  $\ell = 0.004$  m, so that the fracture energy for a given  $\ell$  is

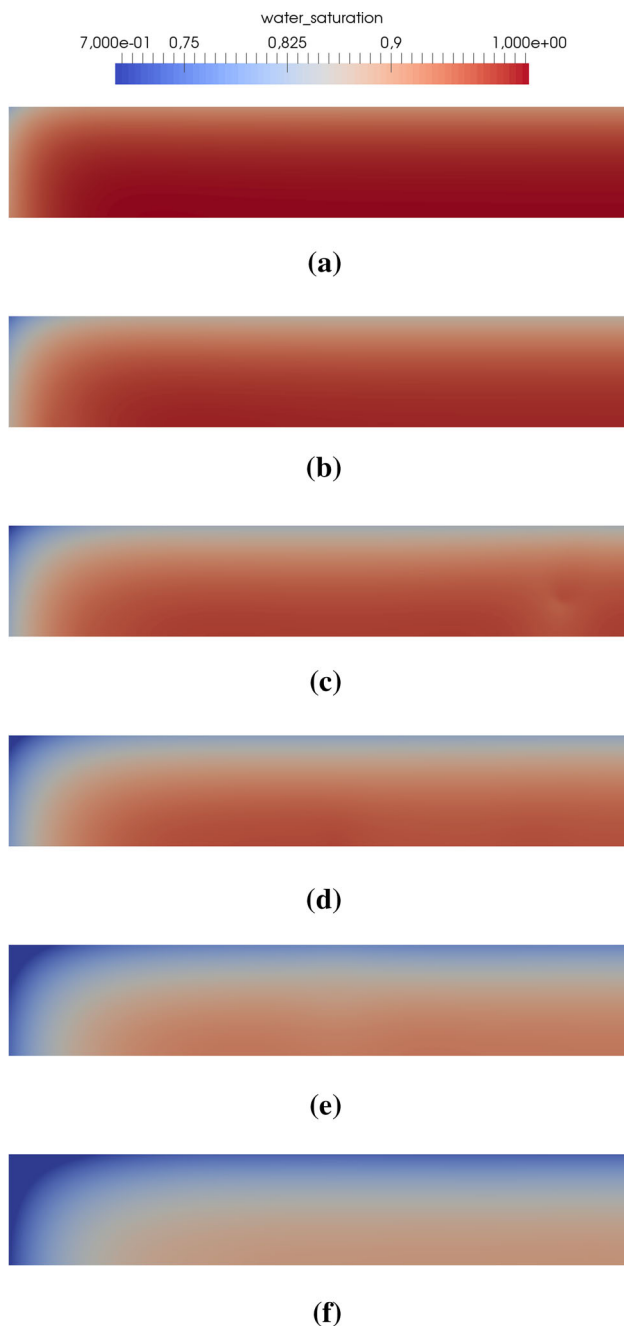


**Fig. 9** Water saturation distribution in the reference specimen subject to drying flux  $\bar{q} = 6 \times 10^{-7}$  m/s at **a**  $t = 15$  min, **b** 30 min, **c** 45 min, **d** 60 min, **e** 90 min and **f** 120 min

doubled. As expected, the crack at the upper drying surface occurs later in comparison to the reference case with  $\ell = 0.002$  m, Fig. 7a–d. This can be observed in Fig. 11a–d. Furthermore, the transition zone is wider. The upper crack propagates vertically and then curves, Fig. 11d. After approximately 95 min from the beginning of the test, it is observed that the crack at the corner and the upper crack propagate further, Fig. 11e. A second crack from the upper drying

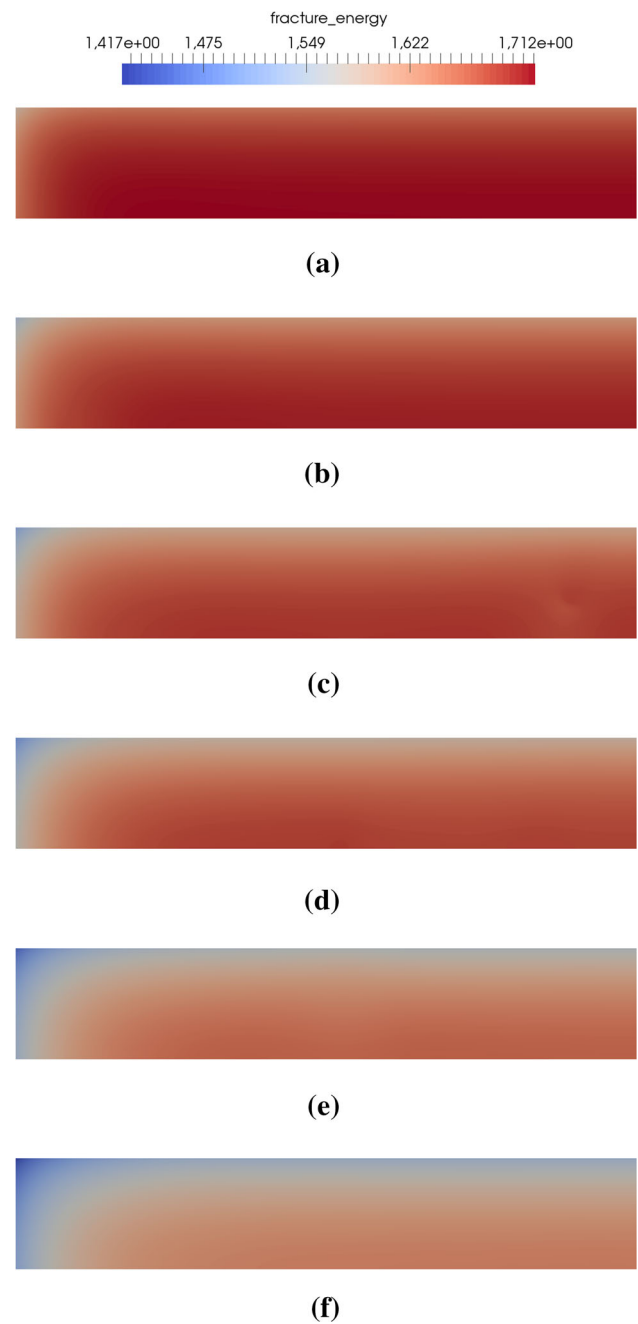


**Fig. 10** Fracture energy (N/m) distribution in the reference specimen subject to drying flux  $\bar{q} = 6 \times 10^{-7}$  m/s at **a**  $t = 15$  min, **b** 30 min, **c** 45 min, **d** 60 min, **e** 90 min and **f** 120 min

surface is observed and the propagation of the crack at the corner is slower in comparison to the reference test, Fig. 11f.

#### 4.3.2 Influence of the mechanical restraint

Péron [4] observed cracks at the corner of his specimens and attributed them to the mechanical restraint. There is no ref-

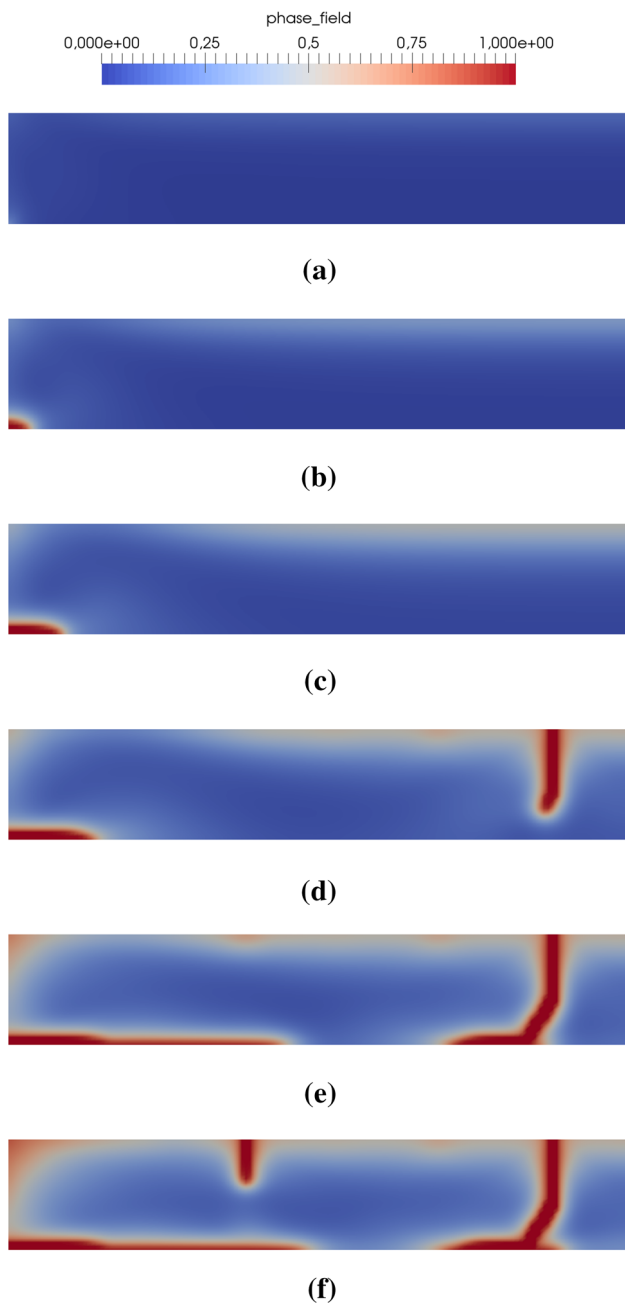


**Fig. 11** Phase-field evolution in the specimen with  $\ell = 0.004$  m, subjected to drying flux  $\bar{q} = 6 \times 10^{-7}$  m/s at **a**  $t = 15$  min, **b** 30 min, **c** 45 min, **d** 60 min, **e** 90 min and **f** 120 min. The first surface crack is observed at  $t \approx 52$  min

erence to such cracks in Stirling's work, probably because the sides of the specimen are hidden. The aim of this section is to analyze the occurrence of cracking at the corner of the specimen in relation to the type of mechanical restraint at the bottom. In the following test, as in the reference test, the vertical component of the displacement of all nodes at the bottom is restrained. However, in the horizontal direction now only one node is restrained to avoid rigid body

motion and all other nodes are left free. The parameters from Table 2 are used. This case can be interpreted as an ideal model with no friction on the bottom surface of the mould. Figure 12 shows the results of this test case. The horizontal shrinkage is larger leading to a different stress distribution in comparison to the fully constrained simulation. On the other hand, the vertical shrinkage is slightly smaller. The suction increases and consequently the horizontal stresses increase. The region with uniform stress field is prone to phase-field evolution. Although the phase-field does not localize up to 60 min, it is possible to recognize its slight uniform increase on the upper layer, Fig. 12a–d. Localization occurs close to the left end of the specimen due to larger strain development after 70 min of the start of the test. Figure 12e shows the developed cracks at 90 min. The first crack initiates and approximately 23 min later, the onset of a second crack is observed. The third crack appears shortly after and a fourth crack initiates at the symmetry line approximately at 115 min and propagates further, Fig. 12f. The crack at the corner of the specimen does not initiate, confirming that the occurrence of such cracks is related to the mechanical horizontal restraint at the bottom of the specimen. It is also important to note that in this test case none of the cracks propagates through the specimen.

#### 4.3.3 Influence of the drying flux

Here we perform a numerical test applying a higher drying flux  $\bar{q} = 1 \times 10^{-6}$  m/s. The phase-field distribution at different time steps is shown in Fig. 13. It is possible to observe an increase of the number of secondary cracks with respect to the reference case solved with a lower flux ( $\bar{q} = 6 \times 10^{-7}$  m/s), which is in agreement with the observations from Stirling [5].

At 15 min from the start of the test, cracking at the corner of the specimen is observed, Fig. 13a. After 20 min of drying, two small cracks are initiated at the upper surface. Shortly after, these cracks propagate further. At 25 min, the main cracks and three other secondary cracks are present along with a larger crack at the corner than in the reference test at the same time step, Figs. 13b and 7b for comparison. The crack at the corner does not propagate further. At 45 min, the first two main cracks are almost completely propagated, Fig. 13c, while with lower flux the first vertical cracks had appeared at about 41 min. Further cracks appear and propagate as visible in Fig. 13d, e. The degradation of the left extremity of the specimen is already observed at 86 min and its region extends further until the end of the test. Figure 13e, f denote a very advanced stage of the simulation where the specimen has failed and is only reported for consistency with the other figures. In summary, the higher flux leads to an earlier appearance of



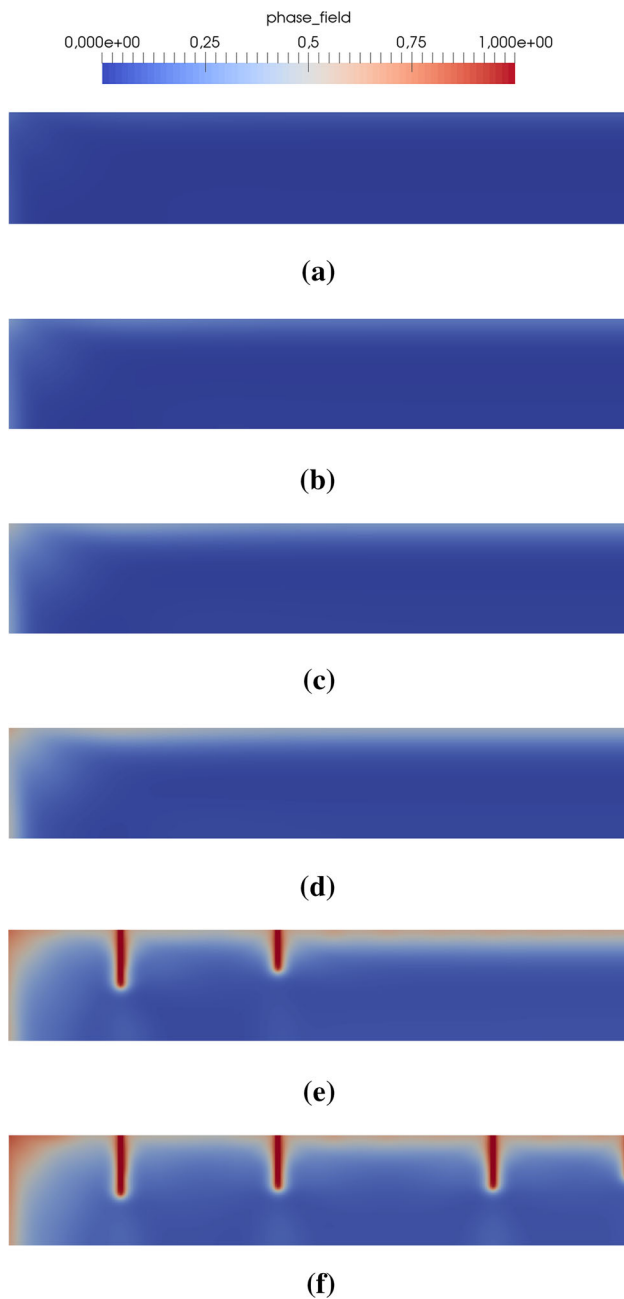


**Fig. 12** Phase-field evolution in the single point restrained specimen configuration at **a**  $t = 15$  min, **b** 30 min, **c** 45 min, **d** 60 min, **e** 90 min, and **f** 120 min. The first surface crack is observed at  $t = 70$  min

cracks and to a more extensive cracking. Also, it favors the crack propagation from the upper surface over the corner crack.

#### 4.3.4 Step-wise application of the drying flux

The next numerical example simulates an experimental desiccation test where the specimen is inserted in a compart-

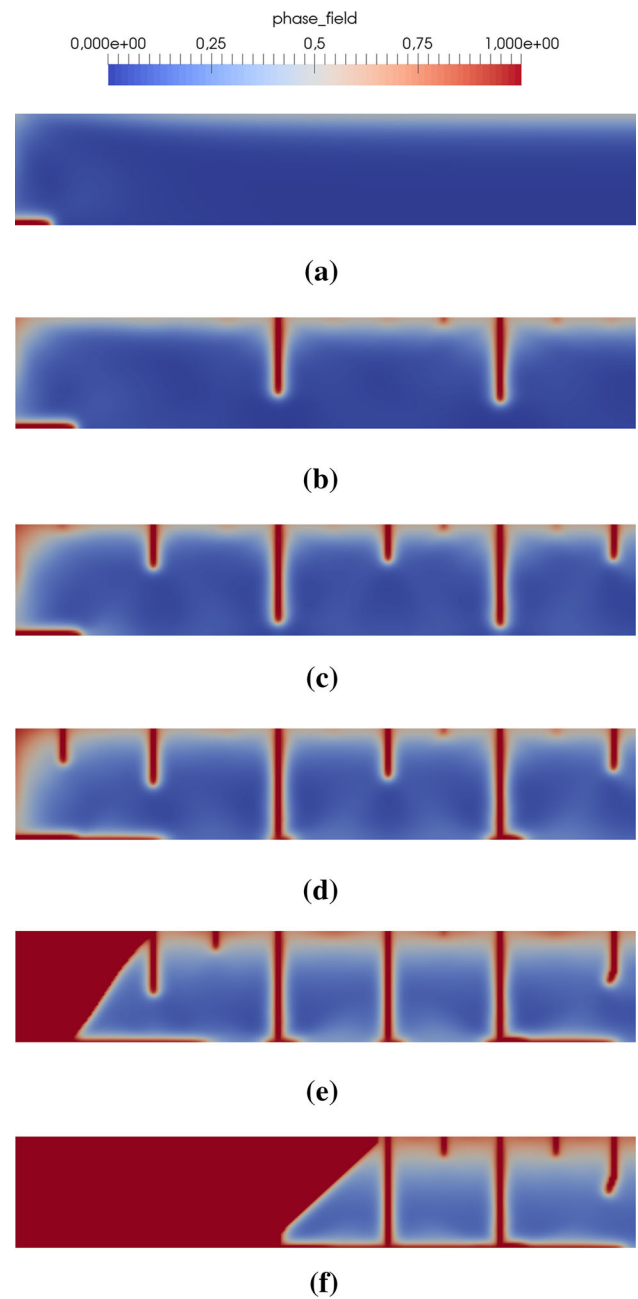


**Fig. 13** Phase-field evolution in the specimen with high drying flux  $\bar{q} = 1 \times 10^{-6}$  m/s at **a**  $t = 15$  min, **b** 30 min, **c** 45 min, **d** 60 min, **e** 90 min and **f** 120 min. The first surface crack is observed at  $t \approx 20$  min

ment [1]. In this case, only the upper surface of the specimen is allowed to dry and only after the occurrence of lateral shrinkage the specimen loses water from the sides. To model this test we introduce the idea of step-wise drying flux. First, a drying flux is imposed at the upper surface of the specimen and, when lateral shrinkage is observed ( $t \approx 60$  min), a second drying flux is applied to the lateral sides of the sample.

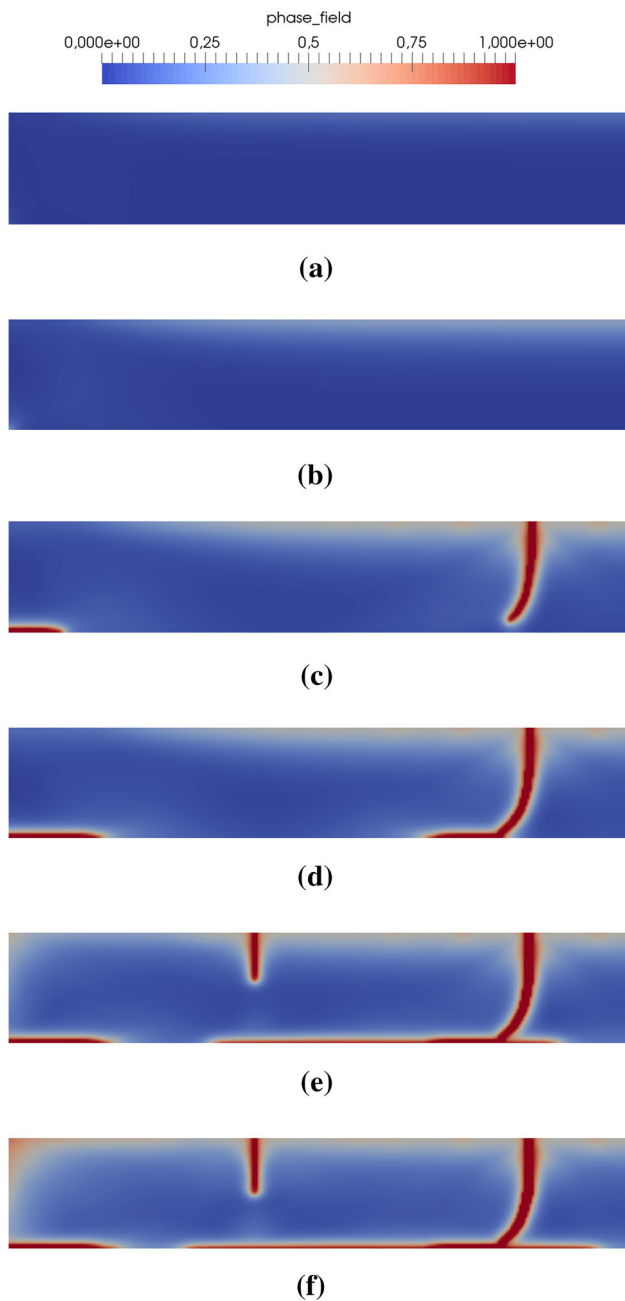


**Fig. 14** Phase-field evolution in the specimen with step-wise drying flux  $\bar{q} = 6 \times 10^{-7}$  m/s at **a**  $t = 15$  min, **b** 30 min, **c** 45 min, **d** 60 min, **e** 90 min and **f** 120 min. The first surface crack is observed at  $t \approx 41$  min

Comparing the results of this simulation with the results from the reference test, we notice that the extension of the crack at the corner diminishes. At  $t \approx 41$  min, this extension corresponds to less than half of that observed in the standard test, Fig. 14a. The phase-field at the upper surface localizes 10 s later in comparison to the reference case and the location of this crack is shifted to the left. This can be explained due to the smaller extension of the crack at the

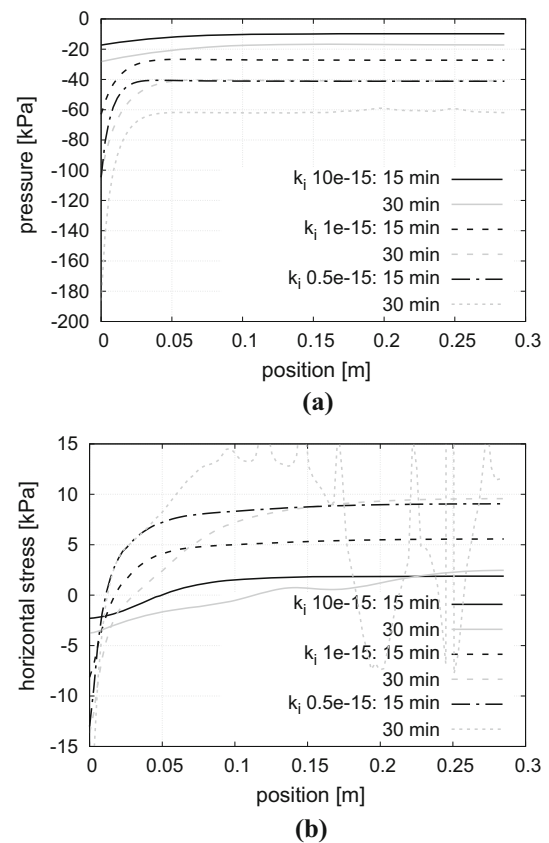


**Fig. 15** **a** Pressure and **b** horizontal stress distribution along upper surface at 15 and 30 min with  $k_i = \{0.5, 1, 10\} \times 10^{-15} \text{m}^2$

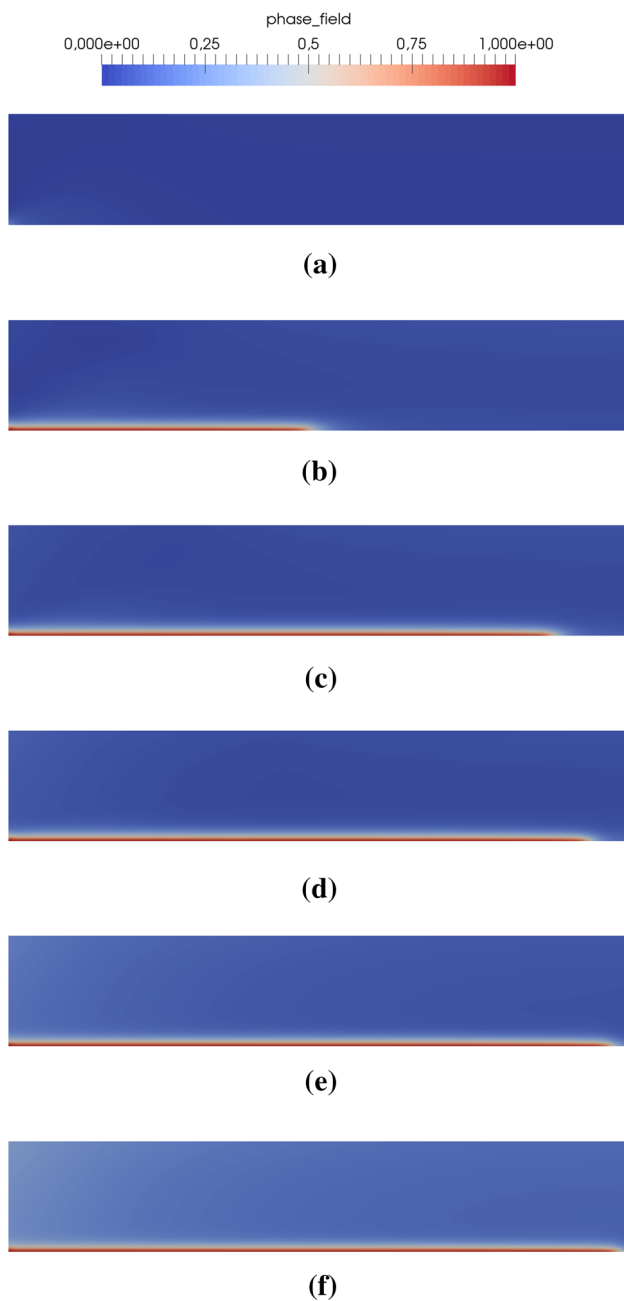
corner leading to a different stress distribution along the specimen. Short before 1 h of test, the crack has fully propagated through the specimen, Fig. 14c–d. At approximately 80 min, a second crack starts at the upper surface. The crack at the corner and the first crack propagate further as shown in Fig. 14e–f.

#### 4.3.5 Influence of the intrinsic permeability

The intrinsic permeability is a material property that varies in a wide range due to the grain structure and the compaction processes of the experimental tests. In order to understand its influence on cracking, we perform three case studies taking the values  $k_i = \{0.5, 1, 10\} \times 10^{-15} \text{m}^2$ . The intermediate value was already used in the reference test described in Sect. 4.2.

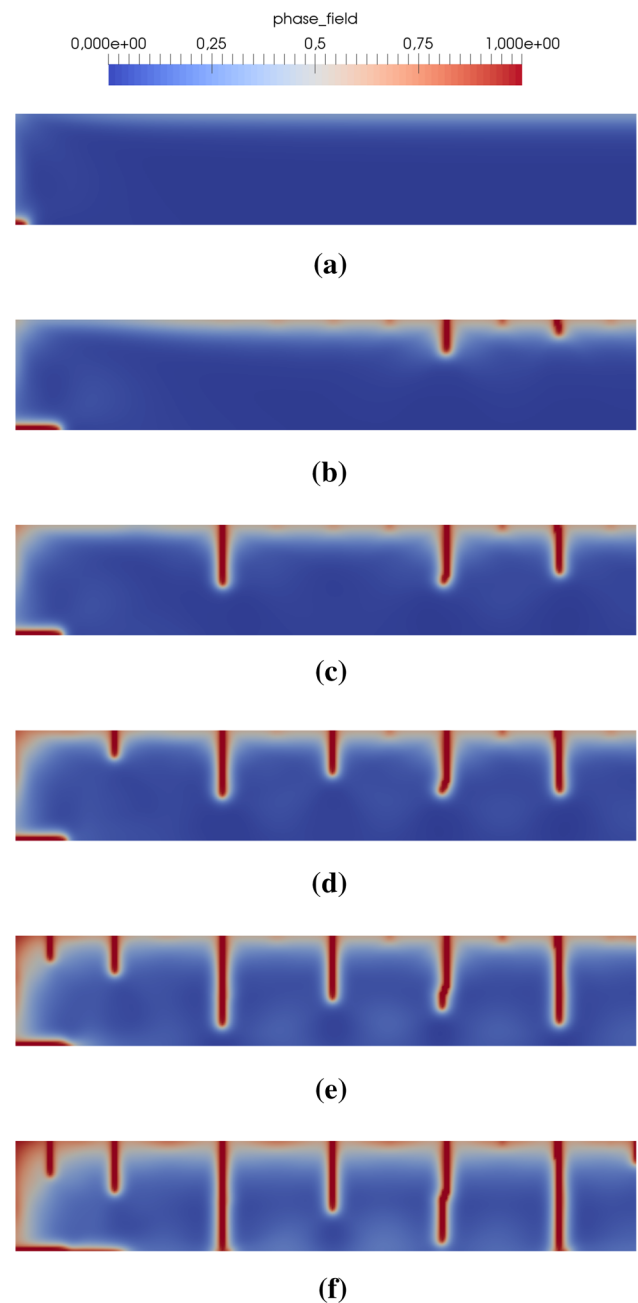
In a material with higher permeability, the water flows more easily in comparison to a material with lower permeability and, consequently, the pressure gradients are lower. Smaller permeability leads to larger pressure gradients which are expected to accelerate cracking.

Figure 15 shows the distributions of the water pressure (a) and horizontal stress (b) along the upper surface at 15 and



**Fig. 16** Phase-field evolution in the specimen with intrinsic permeability  $k_i = 10 \times 10^{-15} \text{m}^2$  and drying flux  $\bar{q} = 6 \times 10^{-7} \text{m/s}$  at **a**  $t = 15 \text{min}$ , **b**  $30 \text{min}$ , **c**  $45 \text{min}$ , **d**  $60 \text{min}$ , **e**  $90 \text{min}$  and **f**  $120 \text{min}$ . Crack initiates and propagates only at the bottom of the specimen

30 min. The higher the permeability, the higher the value of the water pressure. The water pressure increases in absolute value with time. The horizontal stress distribution follows the opposite tendency as shown in Fig. 15b. The lower the permeability, the higher the value of the horizontal stress. At 15 min, a positive uniform horizontal stress distribution



**Fig. 17** Phase-field evolution in the specimen with intrinsic permeability  $k_i = 0.5 \times 10^{-15} \text{m}^2$  and drying flux  $\bar{q} = 6 \times 10^{-7} \text{m/s}$  at **a**  $t = 15 \text{min}$ , **b**  $30 \text{min}$  onset of first upper crack, **c**  $45 \text{min}$ , **d**  $60 \text{min}$ , **e**  $90 \text{min}$  and **f**  $120 \text{min}$ . The crack at the corner of the specimen remains limited

is observed. The stress increases with time for the specimens with  $k_i = \{0.5, 1\} \times 10^{-15} \text{m}^2$ . On the other hand, since the specimen with lower permeability suffers early detachment from the bottom, the stress decreases, becomes negative and no main cracking is expected to occur. This condition is comparable to a free desiccation test, where

no cracks initiating on the upper surface are observed in the experiments. The crack at the corner of the specimen and its propagation along time can be confirmed in Fig. 16.

We expect a larger number of cracks in the specimen with the lowest permeability  $k_i = 0.5 \times 10^{-15} \text{ m}^2$ . Here, the pressure gradients within the specimen are higher, corresponding to a desiccation crust in the specimen. Already after 30 min from the start of the test, several localization areas can be observed, Fig. 17a. From these, two cracks emerge, Fig. 17b. The two cracks propagate further along the specimen and we observe a third localization area at 48 min. The three cracks propagate together and more localization areas are observed, Fig. 17d, e. A total of six cracks is registered after the first hour, Fig. 17f. It can be observed that the crack at the corner is a secondary crack that does not extend after the onset of the first crack. The crack at the extremity of the specimen propagates further due to high pressure in this region.

## 5 Conclusions

A new computational framework for the modeling of flow, deformation and cracking in variably saturated porous media was developed as a coupled  $\mathbf{u}$ - $p_w$ - $d$  model and presented in this work. The coupling between the poromechanical problem and the phase-field evolution was realized through the generalized effective stress. Furthermore, the fracture energy was expressed as a function of the water content. The model was discretized with the finite element method and solved using a staggered solution scheme. First, the poromechanical  $\mathbf{u}$ - $p_w$  model was verified by solving a numerical benchmark problem (Liakopoulos test), followed by the numerical solution of the coupled  $\mathbf{u}$ - $p_w$ - $d$  system applied to the desaturation of a restrained column inspired from the previous verification problem. Then, a constrained desiccation test inspired by experiments in the literature was modeled, obtaining numerical results qualitatively consistent with the experimental results and with observations from the literature. In particular, the model was able to predict the initiation and propagation of primary and secondary cracks through the specimen. Furthermore, a series of sensitivity tests were performed, giving an overview on the influence of material and hydrological properties such as the fracture energy and permeability on the development of the primary variables. The influence of the boundary conditions related to drying and mechanical restraint was also studied.

It was found that the permeability has a significant influence on crack development. The decrease of the permeability

leads to a larger number of desiccation cracks. This fact can be explained by the higher pressure gradients developed within the medium. Conversely, the increase of the permeability leads to a more uniform pressure distribution, hence to a smaller desiccation crust.

The type of mechanical restraint also plays a significant role. In presence of horizontal restraint at the bottom of the specimen, e.g. due to friction, a corner crack develops and, upon propagation, leads to detachment of the specimen from the mould. In absence of such restraint, a very different crack pattern is obtained.

The drying flux boundary condition is an important factor in controlling the number of cracks. Its increase leads to more secondary cracks and less extensive cracking at the corner of the specimen. Another important aspect on the study of crack development is the effect of the step-wise application of the drying flux.

This work proposed an expression to compute the fracture energy as a function of the water content in the specimen and therefore of the degree of saturation. This modification should lead to a more physical modeling of cracking induced by drying, since the fracture energy reduces with drying and cracks become more likely to occur. Fracture energy measurements by experiments at different water contents should be used for validation or improvement of the proposed equation. The available data [1,4] are not sufficient for this purpose, as they lead to a wide variation of the computed fracture energy. On the other hand, this parameter is crucial for the correct evolution of the phase-field variable. The need arises for careful and extensively documented experimental studies which can be used for quantitative validation of the numerical phase-field model. Due to the necessity of fine meshes, further research is needed on adaptive mesh refinement to enhance the efficiency of the computations.

**Acknowledgements** We would like to acknowledge the funding provided by the German Research Foundation DFG GRK-2075.

## Appendix A

In order to check the accuracy of the results reported in the main body of the paper, which were obtained using an explicit staggered approach, the reference test and the test case with  $k_w = 0.5 \times 10^{-15} \text{ m}^2$  were recomputed with 10 staggered iterations. The results are shown in this section. The comparison with the explicit cases (Figs. 7, 17) show that the phase-field evolution is not strongly affected by the number of staggered iterations (Figs. 18, 19).

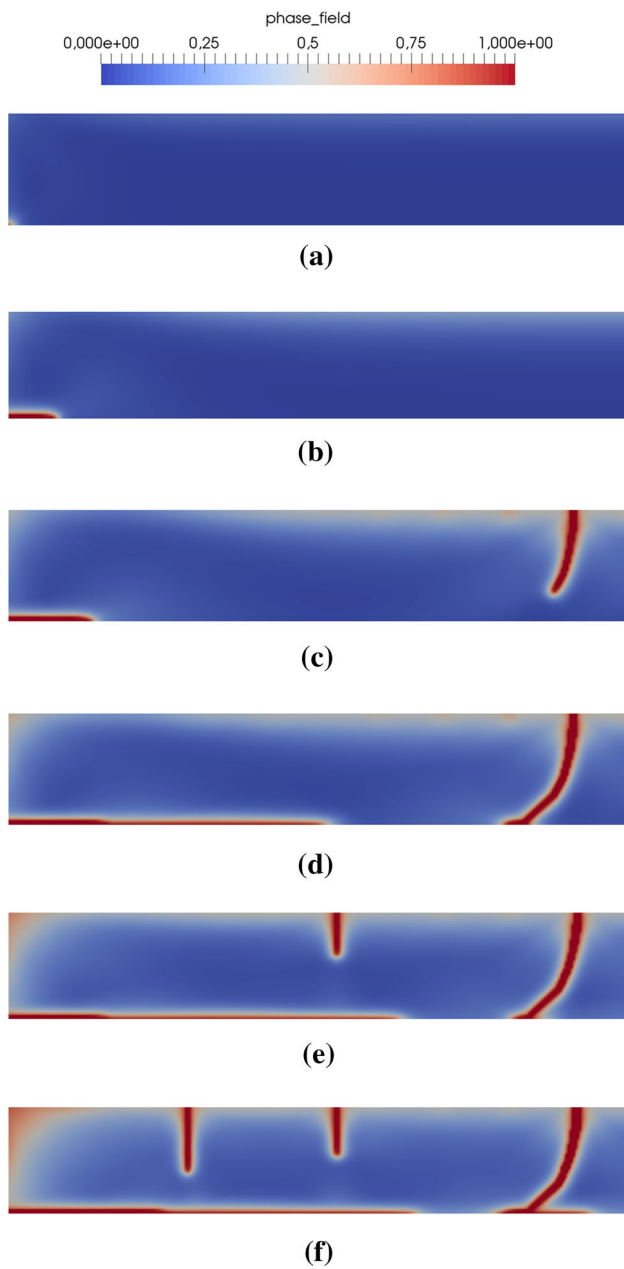


**Fig. 18** Phase-field evolution in the reference specimen subject to drying flux  $\bar{q} = 6 \times 10^{-7}$  m/s computed with 10 staggered iterations at **a**  $t = 15$  min, **b** 30 min, **c** 45 min, **d** 60 min, **e** 90 min and **f** 120 min. These results can be compared with the results in Fig. 7

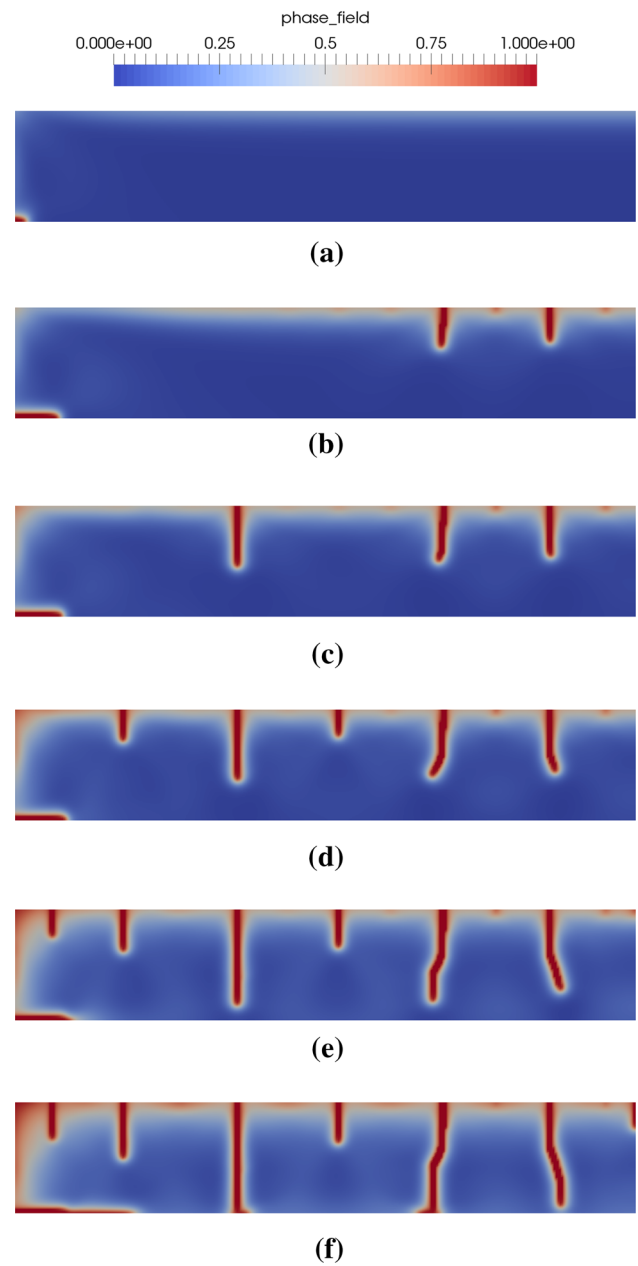


**Fig. 19** Phase-field evolution in the specimen with intrinsic permeability  $k_i = 0.5 \times 10^{-15} \text{m}^2$  and drying flux  $\bar{q} = 6 \times 10^{-7}$  m/s computed with 10 staggered iterations at **a**  $t = 15$  min, **b** 30 min, **c** 45 min, **d** 60 min, **e** 90 min and **f** 120 min. These results can be compared with the results in Fig. 17



## References

- Lakshmikantha MR (2009) Experimental and theoretical Analysis of cracking in drying soils. PhD thesis, Universitat Politècnica de Catalunya
- Lakshmikantha MR, Prat PC, Ledesma A (2012) Experimental evidence of size effect in soil cracking. *Can Geotech J* 49(3):264–284
- Trabelsi H, Jamei M, Zenzri H, Olivella S (2012) Crack patterns in clayey soils: experiments and modeling. *Int J Numer Anal Meth Geomech* 36:1410–1433
- Péron H (2009) Desiccation cracking of soils. PhD thesis, École Polytechnique Fédérale de Lausanne
- Stirling RA (2014) Multiphase modelling of desiccation cracking in compacted soil. PhD thesis, Newcastle University
- Costa SM (2009) Study of desiccation cracking and fracture properties of clay soils. PhD thesis, Monash University
- Lecocq N, Vandewalle N (2002) Experimental study of cracking induced by desiccation in 1-dimensional systems. *Eur Phys J E* 8:445–452. doi:10.1140/epje/i2002-10040-2
- Musielak G, Śliwa T (2012) Fracturing of clay during drying: modelling and numerical simulation. *Transp Porous Media* 95(2):465–481
- Murray I, Tarantino A, Francescon F (2014) Crack formation in clayey geomaterials subjected to tensile (total) stress. *Unsaturated Soils: Research & Applications*, pp 823–828
- Murray I, Tarantino A, Gérard P, Francescon F (2014) Desiccation cracking in clay forms subjected to non-uniform hydraulic and mechanical boundary conditions. In: Khalili N, Russell AR, Khoshghalb A (eds) *Unsaturated Soils: Research & Applications*. CRC Press, pp 829–834. doi:10.1201/b17034-118
- Péron H, Hueckel T, Laloui L, Hu L-B (2009) Fundamentals of desiccation cracking of fine-grained soils: experimental characterisation and mechanisms identification. *Can Geotech J* 46(10):1177–1201
- Simoni L, Schrefler BA (2014) Multi field simulation of fracture. *Adv Appl Mech* 47(C):367–519
- Ayada R, Konrad J-M, Soulié M (1997) Desiccation of a sensitive clay: application of the model CRACK. *Can Geotech* 34:943–951
- Prat PC, Ledesma A, Cabeza L (2002) Drying and cracking of soils: numerical modeling. In: *Proceedings of the 8th international conference on numerical models in geomechanics*, Rome, Italy, pp 10–12
- Gerard P, Murray IW, Tarantino A, Francescon F (2015) On the mechanism for desiccation cracks initiation in clayey materials. In: *Computer methods and recent advances in geomechanics-14th international conference of international association for computer methods and recent advances in geomechanics*, IACMAG 2014, pp 1327–1331
- Bui HH, Nguyen GD, Kodikara J, Sanchez M (2015) Soil cracking modelling using the mesh-free sph method. In: *12th Australia New Zealand conference on geomechanics (ANZ 2015)*
- Kodikara J, Costa S (2013) Desiccation cracking in clayey soils: mechanisms and modelling. In: *Multiphysical testing of soils and shales*. Springer, pp 21–32
- Stirling RA, Davie CT, Glendinning S (2015) Multiphase modelling of desiccation cracking in the near-surface of compacted soils. In: *Proceedings of the 16 th European conference on soil mechanics and geotechnical engineering*. Edinburgh, pp 2311–2316
- Peron H, Laloui L, Hu L-B, Hueckel T (2013) Formation of drying crack patterns in soils: a deterministic approach. *Acta Geotech* 8(2):215–221
- Hirobe S, Oguni K (2016) Coupling analysis of pattern formation in desiccation cracks. *Comput Methods Appl Mech Eng* 307:470–488
- Francfort GA, Marigo J-J (1998) Revisiting brittle fracture as an energy minimization problem. *J Mech Phys Solids* 46(8):1319–1342
- Bourdin B, Francfort GA, Marigo J-J (2000) Numerical experiments in revisited brittle fracture. *J Mech Phys Solids* 48(4):797–826
- Ambati M, Gerasimov T, De Lorenzis L (2014) A review on phase-field models of brittle fracture and a new fast hybrid formulation. *Comput Mech* 55:383–405
- Mikelić A, Wheeler MF, Wick T (2014) A phase-field method for propagating fluid-filled fractures coupled to a surrounding porous medium. *SIAM Multiscale Model Simul* 13(1):367–398
- Mikelić A, Wheeler MF, Wick T (2015) Phase-field modeling of a fluid-driven fracture in a poroelastic medium. *Comput Geosci* 19:1–25
- Heider Y, Markert B (2016) A phase-field modeling approach of hydraulic fracture in saturated porous media. *Mech Res Commun* 80:38–46
- Zienkiewicz OC, Chan AHC, Pastor M, Schrefler BA, Shiomi T (1999) *Computational geomechanics—with special reference to earthquake engineering*. Wiley, Chichester
- Lewis RW, Schrefler BA (1998) *The finite element method in the static and dynamic deformation and consolidation of porous media*
- Schrefler BA, Sanavia L, Majorana CE (1996) A multiphase medium model for localisation and postlocalisation simulation in geomaterials. *Mech Cohesive-frictional Mater* 1(1):95–114
- Nuth M, Laloui L (2008) Effective stress concept in unsaturated soils: clarification and validation of a unified framework. *Int J Numer Anal Meth Geomech* 32(7):771–801
- Schrefler BA (1984) *The Finite Element Method in Soil Consolidation (with applications to Surface Subsidence)*. PhD thesis, University College of Swansea
- Gray WG, Hassanizadeh SM (1991) Unsaturated flow theory including interfacial phenomena. *Water Resour Res* 27(8):1855–1863
- van Genuchten MT (1980) A closed-form equation for predicting the hydraulic conductivity of unsaturated soils. *Soil Sci Soc Am J* 44:892–898
- Kuhn C, Noll T, Müller R (2016) On phase field modeling of ductile fracture. *GAMM-Mitteilungen* 39(1):35–54
- Wu T, De Lorenzis L (2016) A phase-field approach to fracture coupled with diffusion. *Comput Methods Appl Mech Eng* 312:196–223
- Miehe C, Hofacker M, Welschinger F (2010) A phase field model for rate-independent crack propagation: Robust algorithmic implementation based on operator splits. *Comput Methods Appl Mech Eng* 199(45):2765–2778
- Freddi F, Royer-Carfagni G (2010) Regularized variational theories of fracture: a unified approach. *J Mech Phys Solids* 58(8):1154–1174
- Amor H, Marigo J-J, Maurini C (2009) Regularized formulation of the variational brittle fracture with unilateral contact: numerical experiments. *J Mech Phys Solids* 57(8):1209–1229
- Miehe C, Welschinger F, Hofacker M (2010) Thermodynamically consistent phase-field models of fracture: variational principles and multi-field fe implementations. *Int J Numer Meth Eng* 83:1273–1311
- Stirling RA, Simpson DJ, Davie CT (2013) The application of digital image correlation to brazilian testing of sandstone. *Int J Rock Mech Min Sci* 60:1–11

41. Borden MJ, Verhoosel CV, Scott MA, Hughes TJR, Landis CM (2012) A phase-field description of dynamic brittle fracture. *Comput Methods Appl Mech Eng* 217:77–95
42. Gerasimov T, De Lorenzis L (2016) A line search assisted monolithic approach for phase-field computing of brittle fracture. *Phase field approaches to fracture. Comput Methods Appl Mech Eng* 312:276–303
43. Gross S, Reusken A (2011) *Numerical methods for two-phase incompressible flows*, vol 40. Springer Science & Business Media, New York
44. Bangerth W, Davydov D, Heister T, Heltai L, Kanschä G, Kronbichler M, Maier M, Turcksin B, Wells D (2016) The deal.II library, version 8.4. *J Numer Math* 24:135–141
45. Liakopoulos AC (1964) *Transient flow through unsaturated porous media*. PhD thesis, University of California, Berkeley
46. Gawin D, Sanavia L (2009) A unified approach to numerical modeling of fully and partially saturated porous materials by considering air dissolved in water. *Comput Model Eng Sci* 53(3):255
47. Gawin D, Schrefler BA (1996) Thermo-hydro-mechanical analysis of partially saturated porous materials. *Eng Comput* 13(7):113–143
48. Jommi C, Vaunat J, Gens A, Gawin D, Schrefler BA (1997) Multiphase flow in porous media: a numerical benchmark. *Proc NAFEMS World Congr* 97:1338–1349
49. Sanavia L, Pesavento F, Schrefler BA (2006) Finite element analysis of non-isothermal multiphase geomaterials with application to strain localization simulation. *Comput Mech* 37(4):331–348